UNIVERSITY OF OKLAHOMA

GRADUATE COLLEGE

EVALUATING BOUNDARY LAYER FEATURES IN THE CHEESEHEAD CAMPAIGN AND THEIR CONTRIBUTION TO CONVECTION EVOLUTION DURING THE 19-20 JULY 2019 SEVERE WEATHER OUTBREAK

A THESIS

SUBMITTED TO THE GRADUATE FACULTY

in partial fulfillment of the requirements for the

Degree of

MASTER OF SCIENCE IN METEOROLOGY

By

NOLAN MEISTER
Norman, Oklahoma
2022

EVALUATING BOUNDARY LAYER FEATURES IN THE CHEESEHEAD CAMPAIGN AND THEIR CONTRIBUTION TO CONVECTION EVOLUTION DURING THE 19-20 JULY 2019 SEVERE WEATHER OUTBREAK

A THESIS APPROVED FOR THE
SCHOOL OF METEOROLOGY

BY THE COMMITTEE CONSISTING OF

Dr. Elizabeth Smith, Chair

Dr. Petra Klein

Dr. Scott Salesky

Acknowledgements

It takes a village to create a thesis, and this is no less true during the past few covid-impacted years. I'm grateful for all of the individuals and organizations that have supported me in achieving the goal of attaining my M.S. First and foremost, thank you to Dr. Elizabeth Smith and Dr. Petra Klein, who co-advised me on this project. They afforded me a degree of independence to conduct this research in the way that I saw, but also have been instrumental in ensuring that I knew how this work would fit into the broader science. Advising a student primarily via Google Meets calls cannot have been easy, and I'm thankful that we all figured out how to manage together.

Thank you also to Dr. Scott Salesky, the third member of my committee. He and I have had several conversations at times where I felt lost either trying to contextualize boundary-layer-based results I had found, or where I felt lost about the broader graduate school process. Without the guidance he provided during those conversations, this thesis would have been much more difficult to manage.

Thank you to the various organizations and research grants that made this thesis possible, as well. CHEESEHEAD would not have been possible without the funding provided by the National Science Foundation. My own funding for the past two years would not have been possible without a combination of support from OU CIWRO and NSSL. Furthermore, I could not have studied WoFS verification without help and guidance from WoFS experts within NSSL, most notably Dr. Patrick Skinner and Dr. Brian Matilla.

Thank you also to the friends, students, and colleagues that helped me achieve this work either tangibly or intangibly over the last several years. Dr. Tyler Bell and Dr. Josh Gebauer both saved me from my own coding incompetence at various points during my research. Kelsey Britt provided an example

of object-based verification within WoFS that informed and inspired my own fuzzy logic algorithm. Countless other friends and colleagues have helped me get through my M.S. with encouragement, homework help, and just plain friendship.

Last but certainly not least, thank you to my family for supporting my dream to be a meteorologist for the last two decades. My parents have always pushed me towards making that dream into a goal, and finally a reality. My siblings and extended family have always been an encouraging support system, which is no small thing when I'm the first member of my extended family to leave my home state of Michigan. Finally, thank you to my fiancee Elizabeth, who has borne the brunt of complaints, deadlines, 10-hour coding sessions, and me working through multiple vacations when I needed to. If it takes a village to create a thesis, Elizabeth has been the village's fire department, helping me navigate through a busy time personally and professionally.

Table of Contents

List Of Tables

List Of Figures

Abstract

Interactions between the atmospheric boundary layer and convective storms provide an opportunity for research bridging the two meteorological fields. Despite this, there remains a pervasive sense within the meteorological community that the atmospheric boundary layer (ABL) and convection are two separate fields of research. The CHEESEHEAD 2019 project was conducted in northern Wisconsin to study boundary layer responses to spatial heterogeneities. During the project, a multiple-day severe weather event occurred near and south of the CHEESEHEAD domain from 19-20 July 2019, which was forecasted by the NSSL Warn on Forecast Ensemble System (WoFS) ensemble model. This confluence of factors made the case ideally suited for a cross-discipline study into boundary layer evolution and convection evolution.

Boundary layer evolution was studied by comparing composited characteristics within the boundary layer across two remote profiling datasets — one collected in central Oklahoma in July 2020, and a CHEESEHEAD dataset from Wisconsin in July 2019. It was found that the Oklahoma dataset, despite having a more statically stable boundary layer, was more turbulent than the Wisconsin boundary layer. In Oklahoma a strong nocturnal LLJ developed, with the meridional component developing earlier in the evening than the zonal component. In Wisconsin no evidence of a meridional LLJ was found — however, there was evidence of a weak zonal LLJ. These results show that boundary layer features may vary considerably across spatial regimes, although the scales of those feature variabilities are uncertain from these results.

These characteristics informed the WoFS verification study, which was performed across three regimes of severe weather on 19-20 July. WoFS low-level wind forecasts ahead of a tornadic supercell were compared to a CHEESEHEAD radar wind profiler, which found that WoFS overestimated low-level shear ahead

of the supercell. The second regime was a derecho that merged with the supercell, producing significant wind damage. WoFS wind gust forecasts were too far south with the significant wind potential from this regime, with damaging wind potential aided by a statically unstable boundary layer. The third regime was a line of tornadic severe storms the next morning along a stalled outflow boundary. WoFS forecasted the location of the outflow boundary well, and the boundary's stall was influenced by the LLJ. These results show strengths and weaknesses of WoFS within certain convection regimes. Furthermore, the results of this work contextualize the influence of boundary layer features on convection evolution and show the benefits that forecasters and researchers may glean from considering the two fields in tandem.

Chapter 1

Introduction and Motivation

Atmospheric boundary layer (ABL) phenomena and their impacts on convection evolution present a broad research opportunity. The ABL is influential on the development, maintenance, and hazards associated with convection, while convective features similarly influence ABL evolution. Therefore, it is useful for scientists to jointly study the two. Field projects have been conducted to study the impacts of prominent ABL phenomena such as the nocturnal low-level jet (e.g., Pitchford and London 1962, Maddox 1983, Gebauer et al. 2018, Geerts et al. 2017). More generally, the structure of the ABL and its influence on convection was studied as part of the IHOP project in 2002 (Weckwerth and Parsons 2002). Analysis of observational data has shown that boundaries within the ABL are often favored zones for the initiation of new convection (W. 1982, Wilson and Schreiber 1986). Furthermore, projects such as PECAN (Geerts et al. 2017) have found that these boundaries can be a focus for severe hazards such as damaging winds, flooding potential, and tornadoes (Lin et al. 2021). This study identifies several ways in which boundary layer features may have focused convection initiation or enhanced hazards within a severe weather episode. It is first important to define the boundary layer, its structure, and the ways in which we can identify and evaluate a convective environment before exploring the two concepts in tandem.

1.1 Introduction to Boundary Layer Structure and Comparison Analysis

The atmospheric boundary layer is the lowest 1 to 2 km of the Earth's atmosphere; land-atmosphere interactions determine boundary layer evolution. The ABL is a focal point for meteorological study because it directly impacts human life. There is still much to be learned about land-surface interactions and internal processes within the ABL, and how they shape the overall evolution and structure of the boundary layer.

In the early 1900s, the concept of a boundary layer was first explored within the oceanic boundary layer by Prandtl (1904), with a focus on governing equations of motion within a laminar layer. Early pioneers of modern meteorology realized that flows occurring just below the surface of an ocean have similarities to atmospheric flows occurring just above Earth's surface (land, water, or ice) - with an important difference. While oceanic flows were generally understood to be laminar, the ABL is characterized and influenced by turbulence. Kolmogorov (1941) hypothesized that turbulent flow is composed of eddies on multiple length scales. While most atmospheric flows are characterized by low turbulence magnitudes, the ABL is developed by eddies driven through convective mixing, mechanical mixing, or both. The strength of this mixing, in tandem with the depth of the capping inversion aloft, determines the depth of the ABL, which may range from tens to thousands of meters in height. A mixed layer develops and deepens in the presence of more solar radiation, as the ABL becomes more unstable (Monin and Obukhov 1954).

A conceptual model of the ABL diurnal cycle given by Stull (1988) is shown in Figure 1.1. Convective mixing and deepening of the ABL occurs during the

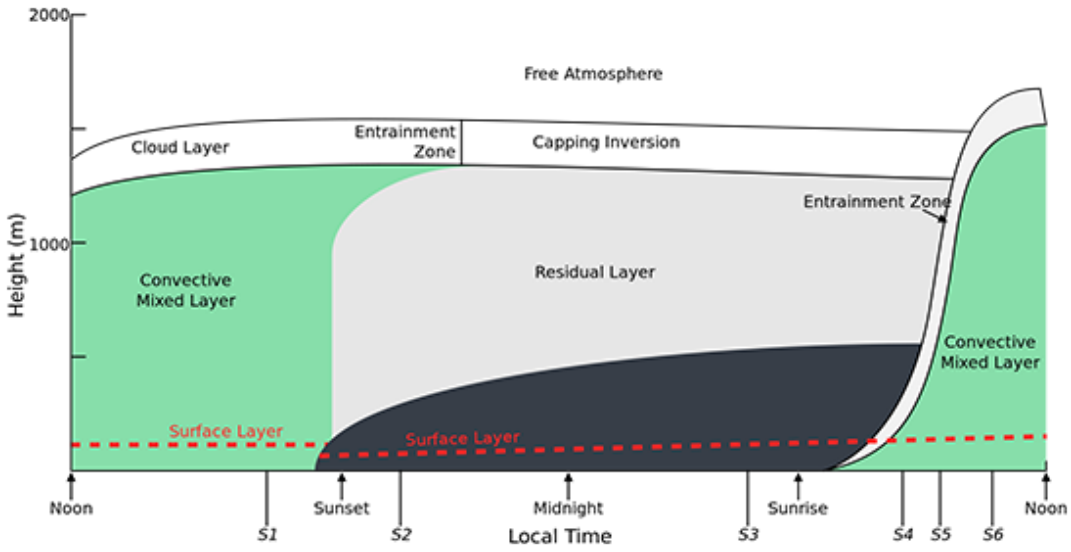

Figure 1.1: Typical atmospheric boundary layer structure and evolution outlined by Stull (1988).

daytime, while a stable ABL develops nearer to the surface following the loss of insolation. Above the stable ABL, a residual mixed layer can be found. At the bottom of the free atmosphere, overshooting convective plumes allow for entrainment of ABL air into the capping inversion during the day.

Observational studies of the ABL have traditionally used in-situ methods of data collection. The Great Plains Field Experiment of 1953 was one of the first of this kind, utilizing in-situ observations and aircraft to measure the wind profile in the ABL. The resulting data helped establish our understanding of the Great Plains nocturnal low-level jet (NLLJ) (Bonner 1968, Carroll et al. 2019 Smith et al. 2019), an important boundary layer phenomenon occurring across the central United States. The development of the rawinsonde allowed for near-instantaneous profiles of temperature, moisture, and winds within the ABL. The utility of these data for this application was proved by Bonner (1968) in compiling a climatology of NLLJs. Sonde data is useful due to the ease and

relatively low cost with which one can be launched. An international network of sondes launched every twelve hours still exists, and field campaigns often still deploy sondes either as focal or auxiliary data collection tools. However, sonde data has limitations for ABL studies. One balloon may take nearly an hour to collect a single vertical profile of the troposphere, during which time conditions may change within the ABL. In addition to not being fixed in time, sondes are not fixed in space — they will drift with the wind as they rise, so that data collected above the launch point frequently occurs at a different latitude and longitude than the original launch point. Ground-based remote sensing instruments have the potential to fill the observational gaps left by in-situ observations of the ABL (Bell et al. 2020a).

Remote sensing platforms such as microwave radiometers and Doppler lidars have the potential to deploy for days or weeks on end, generating long-duration datasets. The utility of this observational method was demonstrated by Zhao et al. (1992) in generating vertical thermodynamic profiles using a microwave radiometer. Doppler radar technology allowed researchers to investigate the velocity characteristics of boundary-layer features such as thunderstorm outflows (Mueller and Carbone 1987). However, radar requires relatively large particles such as hydrometeors to accurately depict velocity fields within the ABL. The Doppler lidar's development allowed scientists to obtain three-dimensional wind components across multiple height ranges within the boundary layer, with its shorter wavelength increasing sensitivity to aerosols making it more reliable for clear-air ABL wind profiles than Doppler radar. Furthermore, Doppler lidar provides ABL profiles with high vertical and temporal resolution (Grund et al. 2001). Combined, these instruments can provide a vertical profile of the same ABL properties that a sonde samples. However, while using sondes, a certain

height level may only be sampled every 30 minutes to 12 hours depending on launch frequency; remote sensing platforms are sensing the atmosphere on a near-constant basis and are capable of providing observations every few minutes or less.

The advantages in ABL observations afforded by remote sensing has led to new research opportunities (Wagner et al. 2019). The University of Oklahoma (OU) designed a mobile remote observational platform, the Collaborative Lower Atmosphere Mobile Profiling System (CLAMPS) in 2015. The CLAMPS platform contains several remote sensing instruments: a microwave radiometer, an Atmospheric Emitted Radiance Interferometer (AERI), and a Doppler lidar. Since 2016, OU and the National Severe Storms Laboratory (NSSL) collaboratively maintain two CLAMPS facilities, CLAMPS1 (OU-NSSL) and CLAMPS2 (NSSL). The University of Wisconsin operates a nearly identical platform, the Space Science and Engineering Center (SSEC) Portable Atmospheric Research Center (SPARC). Other remote sensing platforms exist within the boundary layer field, but CLAMPS and SPARC are unique in their ability to combine kinematic profilers with thermodynamic profilers (in particular, profilers that can retrieve water vapor data) while also maintaining a useful real-time data availability to users.

CLAMPS has been used as a mobile platform during field campaigns such as PECAN (Geerts et al. 2017), CHEESEHEAD and PERiLS to observe ABL phenomena. Smith et al. (2019) studied the NLLJ and discovered its tendency to veer from southerly to westerly overnight, with impacts on overnight ABL evolution. Gebauer et al. (2017) analyzed CLAMPS data depicting a northerly NLLJ in Oklahoma, contrary to the typical considerations of southerly NLLJs on the Great Plains. CLAMPS data are also useful for verifying numerical

simulations of mesoscale phenomena: Flournoy and Coniglio (2019) compared Doppler lidar data with numerical simulations of observed convective features, finding that the simulation and lidar observations both suggested a locally favorable environment for tornadoes ahead of ongoing convection. Other studies have assimilated CLAMPS data into numerical weather prediction models to study its influence on event forecasts (Degelia et al. 2019, Coniglio et al. 2019, Chipilski et al. 2020). Furthermore, ground-based remote sensing instruments provide opportunities to test and intercompare new remote sensing and in-situ instruments in the field (Turner and Löhnert 2021, Bell et al. 2021, Smith et al. 2021).

1.2 Introduction to Convective Environmental Analysis and Verification

Convection is influenced by a variety of factors on multiple scales - internal storm boundary effects on a microscale level, boundary layer features such as gust fronts, or mesoscale to synoptic-scale environmental features. Early thunderstorm research focused on the ingredients necessary for the formation of convection. These studies found that organized severe storms require buoyancy and vertical wind shear (Byers and Battan 1949), as well as moisture and a lifting mechanism. This understanding has created a mental model in the minds of scientists and forecasters that allow them to identify regions where convection initiation is likely. Recent studies of severe thunderstorms have focused on mesoscale and boundary-layer features such as outflow boundaries. These features may initiate convection in otherwise unfavorable environments (Lin et al. 2021). It therefore behooves forecasters to have weather models that accurately

depict the placement of such features before the development of convection, so that they may know where the likeliest regions of convection initiation or hazards may be. Two boundaries that will be investigated in this study are a warm front and its role in supercell maintenance and hazards, as well as the motion of an outflow boundary and its role in the initiation of new convection.

In meteorological terms, a front is defined as the transition zone between airmasses of different density or temperature. Fronts were first defined by the Bergen School of Norwegian scientists during the World War I era (Shapiro and Keyser 1990). The so-named Norwegian model of an extratropical low pressure cyclone included both warm and cold fronts, wherein warm or cold airmasses replace the opposite, respectively. Both types of fronts regularly occur within the continental United States east of the Rocky Mountains.

Identification of warm and cold frontal zones has traditionally been the role of operational forecasters. Using hand analysis techniques, forecasters are able to identify frontal boundaries. This is frequently done by using hourly surface observations across a synoptic scale or mesoscale sector. Such methods may take anywhere from 5 to 30 minutes to accurately depict the environment and provide a higher degree of confidence, which is not particularly efficient (McCann and Whistler 2001). Furthermore, data availability, subjective interpretations of what defines the frontal boundary itself, and data latency issues can confound frontal hand analysis such that Sanders and Doswell (1995) stated that subjective frontal analysis was "problematic at best".

In recent years, meteorologists have used computers to create replicable automated methods to find frontal boundaries. Early automated frontal detection methods used thresholds of the Laplacian of a surface parameter. Hewson (1998) used the Laplacian of wet bulb temperature, while Jenkner et al. (2010) and

Schemm et al. (2015) used the Laplacian of equivalent potential temperature. More recently, automated schemes to locate a front use a blend of variables including surface pressure and temperature gradient, such as Parfitt et al. (2017). The popularity of automated frontal analysis is great enough that the NOAA's Weather Prediction Center (WPC) produces an automated continental surface analysis at regular intervals.

The benefits of automated surface analysis of real observations are obvious and largely aligned with the benefits of hand analysis. Analysis of frontal position in models has its own set of strengths and weaknesses. Notably, the ability to forecast frontal features into the near future provides benefit to forecasters, as frontal position is known to influence mesoscale weather impacts (e.g. Corfidi 1998). However, increased lead time comes with the tradeoff of decreased forecast accuracy, as weather models tend to be less accurate with increasing time (Stern and Davidson 2015). Aside from potential benefits to operational forecasters, evaluation of surface features is a critical part of model evaluation (Lee et al. 2019). Frontal placement is important for short-range models to forecast the placement of high-impact rain events (Yue and Gebremichael 2020) as well as potential impacts from severe weather hazards such as large hail or tornadoes that can be focused along a front (Garner 2013). The widely used High Resolution Rapid Refresh (HRRR) model has been verified against observations for individual features (Pichugina et al. 2019, Pinto et al. 2015), as well as over set geographic domains (Pichugina et al. 2019, Lee et al. 2019). These verification studies set a framework to verify new weather models as they are developed and tested for operational use.

The National Severe Storms Laboratory (NSSL) Warn on Forecast (WoFS) model is a short-range convection-allowing model (CAM) composed of an ensemble of 18 individual members. The ensemble members are divided into three boundary-layer parameterization schemes — six members apiece run with the Mellor–Yamada–Janjić (MYJ), Mellor–Yamada–Nakanishi–Niino (MYNN), and Yonsei University (YSU) parameterizations. WoFS is designed as a short-range forecast tool to aid operational forecasters in the event of high-impact mesoscale weather in the United States (Stensrud et al. 2013). To that point, WoFS is run over a mesoscale domain with the boundaries determined by the weather hazard's geographic extent on a given day.

WoFS is experimentally run every thirty minutes and provides output every five minutes. A single run forecasts six hours ahead of the initialization time. WoFS has a horizontal grid resolution of three kilometers, and a variable vertical grid resolution increasing from 100 meters at the surface to one kilometer at the top of the model grid at 10 hPa. Model runs are typically initiated around midafternoon on a given day, and can run through mid-evening. Data produced from WoFS runs include ensemble averages of environmental parameters such as temperature, moisture content, and wind speed and direction at the surface and several fixed pressure levels; vertical profiles at fixed grid points that allow the generation of simulated atmospheric soundings; and individual member data that allow the forecaster to visualize possible convective evolutions, including updraft helicity (UH) and simulated reflectivity data for each ensemble member. Object-based verification of WoFS has been performed using radar and storm-derived features such as reflectivity and UH (Skinner et al. 2018); however, frontal verification of WoFS has not previously been performed.

1.3 The Overlap Between Boundary-Layer and Convection Science

Because of the influence that both ABL features and convective storms have on humans, both subjects have long been an object of research. Various studies have been conducted into how the ABL impacts convection (Weckwerth and Parsons 2002, Du et al. 2020), while other studies have been conducted into how convection impacts the ABL (Huang et al. 2019, Lamraoui et al. 2019). Despite this, there remains a continuing sentiment within members of the meteorological field that the boundary layer and convection constitute two different fields of study. In reality, the two fields are intertwined, with an opportunity for researchers to bridge the gap between the two fields and use information from one field to inform conclusions drawn about the other. Figure 1.2 provides a visual showing both the common conception of major ABL features and convection hazards, as well as how those features and hazards are related.

The CHEESEHEAD project provides an ideal opportunity to seek out the bridge between the two fields of study. The project's intended goals were to investigate ABL responses to surface heterogeneities, collect data to act as a reference point compared to LES simulations, and determine the scales at which those ABL responses to heterogeneities occur. Given the proliferation of mobile platforms like CLAMPS and SPARC, the opportunity exists to compare boundary layer datasets to one another across different locations. The results of this helps our understanding of the variability possible within ABL phenomena, which informs our understanding of possible ABL responses to heterogeneities. In addition to providing boundary layer research opportunities, CHEESEHEAD also provided opportunities for convection research. The intensive, high-density

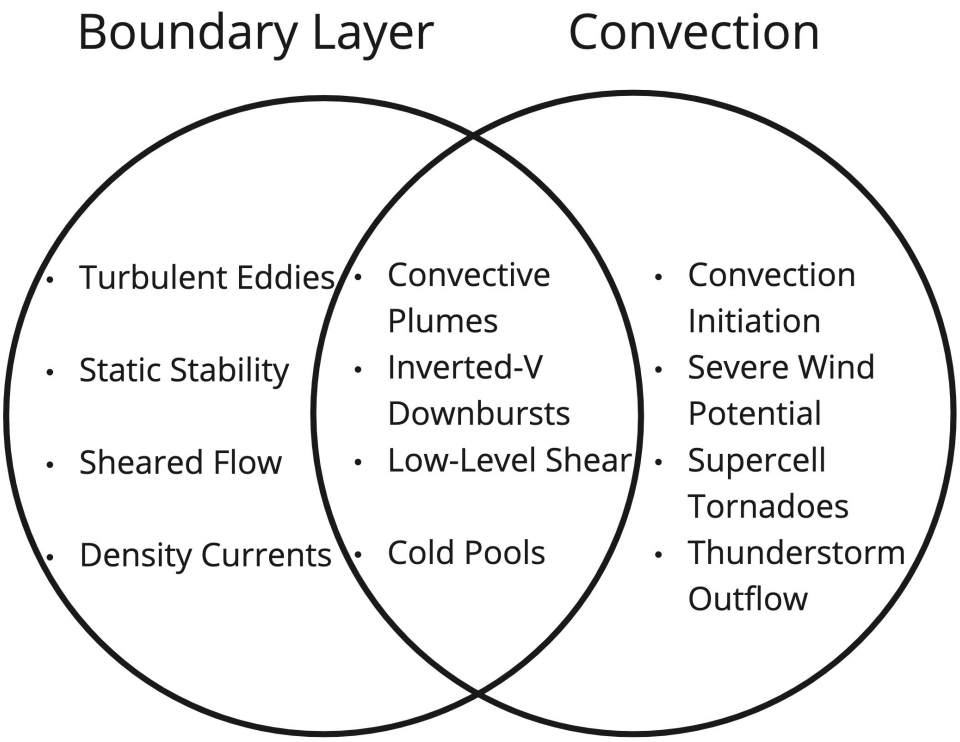

Figure 1.2: A Venn Diagram showing ABL features and convection hazards, as well as the overlapping meteorological features that bridge the two fields.

nature of CHEESEHEAD observations meant that any convection within the domain was detected by an array of instruments including those more typically assessed by NSSL within the Great Plains region. The 19-20 July 2019 severe weather outbreak directly impacted CHEESEHEAD instruments, giving observations of the environment in and around convection.

The WoFS model provides an opportunity to research purely within the convection realm. WoFS datasets are also proliferating, with the model run over 200 times experimentally since 2017. As NSSL prepares for the transition from experimental to operational WoFS data, it is important to understand how the model performs within various regimes of convection. The case that was studied in this work contains several unique advantages for WoFS verification purposes. First of all, as will be discussed in detail later, the 19-20 July 2019 severe weather event that was analyzed occurred with several distinct regimes of convection over the course of one WoFS domain. Therefore, it was possible to verify WoFS for multiple convection modes. Furthermore, the 19-20 July 2019 event occurred within the CHEESEHEAD domain of northern Wisconsin. This provided a unique opportunity to verify WoFS forecasted ABL profiles against actual observed, high-resolution ABL profilers.

These two research objectives, one within the ABL realm and one within the convection realm, have the potential to reinforce the notion that the two fields are separate entities. However, the final motivation for this work is to show the utility in considering both fields in tandem. Given that the CHEESEHEAD project and the 19-20 July 2019 severe weather event overlapped spatiotemporally, ABL features within the CHEESEHEAD domain can be detected and analyzed that influenced convection evolution. These features will be discussed within Chapter 2, with a discussion of convection evolution and hazards within

Chapter 3. Chapter 4 contains a discussion of how long-term ABL evolution in the summer of 2019 in Wisconsin contributed to the specific evolution of storms and their related severe weather hazards across Wisconsin during the 19-20 July 2019 severe weather event.

Chapter 2

Boundary Layer Comparison

2.1 Introduction

Both CLAMPS and SPARC have now been involved in multiple field deployments. Consequently, there is a growing list of long-term datasets in varying conditions gleaned from those platforms. Observational studies focused over one time period in one condition have identified and characterized boundary layer phenomena; for example, Bell et al. (2020b) identified nocturnal boundary layer features such as mountain-valley circulations in complex terrain near Perdigao, Portugal. While such studies were able to identify features such as the aforementioned terrain circulation, these studies occurred earlier in the careers of CLAMPS and SPARC. Thus, there was not a cache of boundary-layer datasets among which boundary layer features could be compared. CLAMPS is now approaching its second decade of field campaigns, and has operated across many regions of the continental United States as well as abroad. The opportunity now exists to study ABL evolution over long durations across different regions, seasons, and land cover regimes. This chapter explores the overall ABL evolution in three different conditions: forested northern Wisconsin during a typical continental summer regime, the same northern Wisconsin forest during the autumn transition, and mixed grassland in central Oklahoma during a humid, subtropical summer regime. In doing so, this thesis continues the work of

using remote sensing platforms to increase our understanding of ABL evolution and phenomena.

The specific impetus for comparing CLAMPS datasets was The Chequamegon Heterogeneous Ecosystem Energy-balance Study Enabled by a High-density Extensive Array of Detectors (CHEESEHEAD) 2019 project. CHEESEHEAD was an intensive field project conducted in northern Wisconsin to study ABL features. The project was specifically designed to "examine how the ABL responds to spatial heterogeneity in surface energy fluxes" (Butterworth et al. 2021). To accomplish this mission, in-situ and remote sensing platforms were arranged within a 10km x 10km array constituting the general experiment domain. With such a high-density network of observational platforms, identifying and analyzing spatial heterogeneities and ABL responses became more possible. CLAMPS and SPARC comprised two of the observational platforms within the CHEESEHEAD project. In addition to CLAMPS and SPARC datasets collected in Wisconsin during CHEESEHEAD, a third dataset was included from CLAMPS in 2020 in Oklahoma from another project. With this third dataset, cross-location comparison of ABL evolution and features became available, which was studied for this project in accordance with CHEESEHEAD research goals.

2.2 Data and Methods

Two CLAMPS trailers were collected simultaneously within the northern Wisconsin CHEESEHEAD domain during the transition season in 2019 (Klein et al. 2020). CLAMPS1 was chosen for the purposes of this research as it had two thermodynamic profilers that operated simultaneously, while CLAMPS2 only had one. Data from both thermodynamic profilers onboard CLAMPS1 could

be used in a thermodynamic retrieval algorithm (mentioned below), increasing confidence in data quality and extending the potential depth of profiles. CLAMPS1 was deployed at Lakeland Airport from 19 September 2019 to 23 October 2019 (see Figure 2.1). Due to outages of several of the relevant platforms during this project, the operational period for this dataset was shortened to the timeframe when all of the platforms were functioning simultaneously, 20 September to 1 October 2019. CLAMPS1 contained a microwave radiometer, as well as an Atmospheric Emitted Radiance Interferometer (AERI), which measured downwelling infrared radiance from 3-19 µm at high spectral resolution. From these downwelling radiance data, it is possible to retrieve thermodynamic characteristics of the atmosphere. While many variables can be retrieved from passive thermodynamic profiler radiance measurements, the two variables focused on in this study are water vapor mixing ratio and potential temperature. These data were retrieved using the method outlined in Turner et al. (2007); in this application, both AERI and microwave data are used to produce combined retrieval products.

As one of the stated goals of the CHEESEHEAD campaign was to obtain datasets to study the impact of tree canopy transition on boundary layer evolution, the CHEESEHEAD campaign began in July of 2019, which is before the CLAMPS deployment period. However, a remotely collected boundary layer dataset was obtained from SPARC in the summer of 2019 (Wagner 2021), which was deployed at the WLEF tower in Park Falls, Wisconsin from 02 July to 11 September (see Figure 2.1). Park Falls is roughly 40 miles west of Lakeland, so local-scale features could have contributed to heterogeneities between the two Wisconsin datasets. However, large-scale features such as possible drought influences on soil moisture would be relatively consistent between Lakeland and

Park Falls. To ensure that the data represented the summertime months of northern Wisconsin prior to onset of seasonal transition, the dataset timeframe was narrowed down to a period from 02 July to 21 July 2019, in order to be similar in length to the CLAMPS fall dataset. SPARC was equipped with an AERI for thermodynamic retrievals. Vertical wind data were also available via the SPARC platform, as it was equipped with a Doppler lidar that ran continuous vertical stares. This permanent stare mode meant that the SPARC platform did not directly measure horizontal wind speeds. Two other lidars, operated by the Karlsrhue Institute of Technology (KIT), were in close proximity at the WLEF tower location. These lidars faced the WLEF tower and performed Range Height Indicator (RHI) scans at elevation angles between 66 and 87 degrees. Combining lidar scans from the SPARC lidar and the two KIT lidars can provide horizontal winds. Wind components at this site were obtained from KIT upon request (Wanner and Mauder 2020) . A top-down schematic of this data collection setup can be found in Figure 2.2, adapted from Wanner and Mauder (2020).

Kinematic profiles from CLAMPS1 were provided by a Halo Streamline XR Doppler lidar. The lidar alternated between collecting horizontal wind profiles and vertical wind profiles. To obtain horizontal wind data, the lidar ran plan position indicator (PPI) scans that were coded into vertical azimuthal displays (VADs). CLAMPS1 collected a PPI at a 70 degree elevation angle every 20 minutes. Vertical wind data were collected by the use of vertical stares, which reached a maximum vertical extent of 8 kilometers with a variable vertical resolution of 18-60 meters. However, data were rarely considered from above 1 or 2 km, because lidar data quality is limited by the depth of high aerosol load within the atmosphere.

Figure 2.1: The location of three major CHEESEHEAD platforms used during this study - CLAMPS1 at Lakeland Airport (red), SPARC at the WLEF tower in Park Falls (blue), and the Prentice radar wind profiler (black).

Figure 2.2: A schematic of the lidar deployment strategy at the WLEF tower in Park Falls during CHEESEHEAD. The blue vertical stare lidar was located within SPARC, while the two orange RHI lidars were operated by KIT, constituting a virtual tower. Adapted from Wanner and Mauder (2020).

Figure 2.3: The location of the Norman, Oklahoma dataset collected in July of 2020 by CLAMPS1. An inset at left shows a local satellite view of Norman, with the black dot showing where the data were collected.

The final dataset analyzed for comparison was collected by CLAMPS1 from 03-21 July 2020 in Norman, Oklahoma (see Figure 2.3). Similar to the year before, CLAMPS1 was outfitted with an AERI, a microwave radiometer, and a Doppler lidar, providing long-duration, high-quality profiles of the thermodynamic and kinematic environment within the boundary layer. The operation strategy for CLAMPS1 is consistent for this period and the Wisconsin fall period, except the frequency of VADs was increased to every 10 minutes during the summer in Oklahoma. The time periods, location, and instruments available for each of these three datasets are shown in Table 2.1.

Statistical characterization of boundary layer evolution was achieved via a compositing method. This method leveraged the strengths of CLAMPS and SPARC while addressing their weaknesses. As previously mentioned, CLAMPS and SPARC are unique in their ability to attain high-resolution, rapid profiles of ABL thermodynamic and kinematic variables for long periods of time. Over

Table 2.1: Information about time periods, location, and observational platforms available during the three deployments analyzed.

Dataset	Platform	Time Frame	Location	Instruments
Wisconsin Summer	SPARC/KIT	02-21 Jul 2019	Park Falls, WI	AERI Doppler lidar (stares, RHI)
Wisconsin Fall	CLAMPS1	20 Sep-01 Oct 2019	Lakeland, WI	AERI MWR Doppler lidar (stares, PPI)
Oklahoma Summer	CLAMPS1	01-21 Jul 2019	Norman, OK	AERI MWR Doppler lidar (stares, PPI)

the course of a single day, these data provide the opportunity to explore ABL phenomena by plotting time-height cross sections of the ABL. Compositing allows researchers to explore how those phenomena occur on average over the course of weeks, enabling a comparison of long-term boundary layer evolution. Furthermore, compositing decreases potential errors and the impact of outlier cases involved in single observations. The retrieval method required to obtain thermodynamic characteristics can have large uncertainty associated with a single observation. Compositing allows a researcher to have an average of dozens of observations. In the event that retrieved data errors were randomly clustered about the true observation, compositing allows for reduced margins of error. In any case, the uncertainties associated with any one observation should not have an out-sized impact on the composite.

The datasets were studied across the length of each deployment period within the ABL. Thermodynamic data were studied up to 2 km; however, because Doppler lidar returns often had poor signal-to-noise ratios above 1 km, kinematic data were only studied to that height. Hourly averages across the entire deployment period of the studied atmospheric variables were then taken at each height bin, giving a time-height cross section of mean boundary layer evolution throughout the day (shown in Figures 2.4 and 2.5. Atmospheric variables studied using the compositing method were derived from retrieved data and include atmospheric static stability, vertical velocity variance, and horizontal moisture transport.

Static stability is the vertical gradient in potential temperature, as shown in Equation 2.1

$$\frac{\partial \theta}{\partial z} = \frac{\theta_{higher} - \theta_{lower}}{z_{higher} - z_{lower}}, \tag{2.1}$$

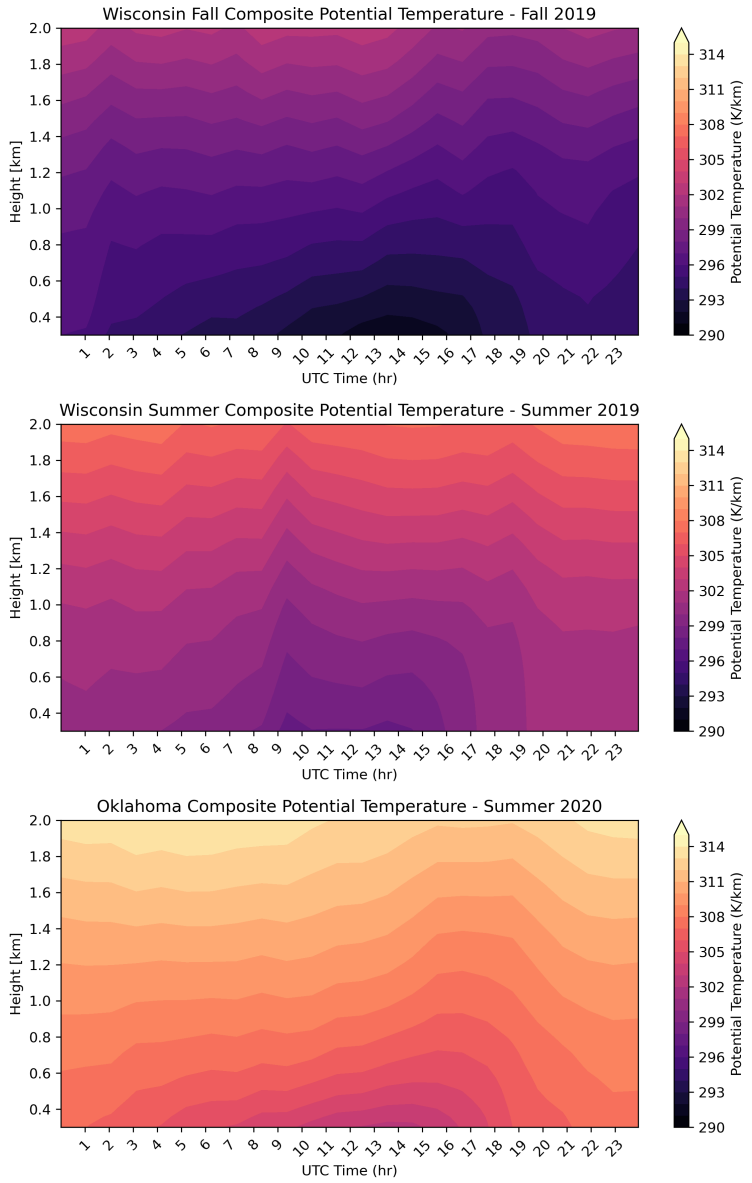

Figure 2.4: Composite potential temperature from Wisconsin in the fall (top), Wisconsin in the summer (middle), and Oklahoma in the summer (bottom).

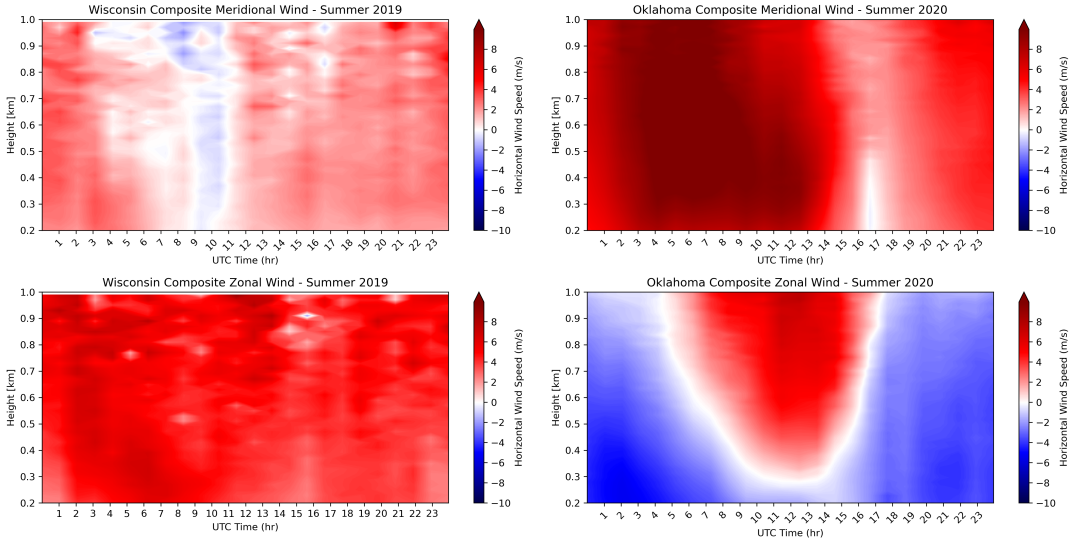

Figure 2.5: Composite horizontal wind components from Wisconsin (left) and Oklahoma (right) in the summer.

where θ is potential temperature and z is height.

Greater static stability values represent areas where potential temperature is increasing more rapidly with height. Static stability nearer zero within the ABL leads to convection and turbulence within the ABL. An example of the compositing process is shown in Figure 2.6: an initial day's worth of potential temperature data is shown, followed by the composite of all potential temperature data, followed by the composite of static stability for the dataset. This follows the methodology employed throughout this research. Note: composite static stability was calculated by taking the vertical gradient of composite potential temperature. To illustrate day-to-day variability of static stability, the standard deviation of daily static stability fields was computed. The combination of composite means and composite standard deviations allow for an overall characterization of ABL static stability as well as day-to-day variability.

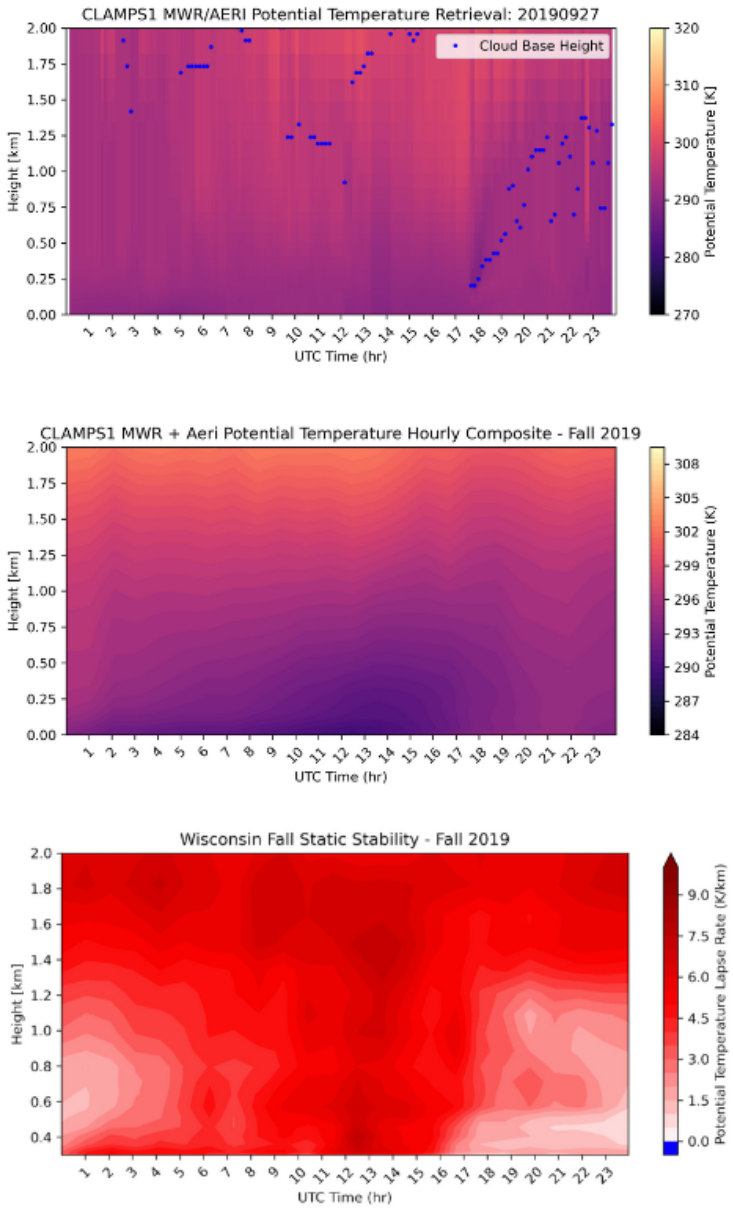

Figure 2.6: An example of the compositing process for static stability, showing the progression from a single day's potential temperature field within the ABL (top) to the composite of all potential temperature within the dataset (middle) to composite static stability (bottom).

Vertical velocity variance represents the fluctuation of vertical wind speed observations from the long-term mean and is expressed as

$$\sigma_w^2 = \sum \frac{w'^2}{n}, \tag{2.2}$$

where σ_w^2 is the vertical velocity variance and w' is the fluctuating component of the vertical velocity. Magnitudes of vertical velocity variance constitute a reasonable approximation for the level of turbulence within a layer (Bonin et al. 2016). Huang et al. (2017) noted that vertical velocity variance provides a more reliable depth of the ABL than using wind shear measurements. Vertical velocity variance from each Doppler lidar stare dataset was calculated using a modified version of the method described by Lenschow et al. (1980, 2012) following closely to the method of Bonin et al. (2016). This method flagged and excluded data from outside the ABL as too noisy to produce accurate vertical velocity variance data. Thus, within the compositing method, all height levels and times that had less than five total observations from across the dataset were excluded from the composite means on the grounds that there were insufficient data for accurate composite values.

Moisture transport was calculated by multiplying water vapor mixing ratio at a time and height by the corresponding u or v wind component at that height and time. Moisture transport is calculated in Equations 2.3 and 2.4,

$$T_u = w_{vap} * u, \tag{2.3}$$

$$T_v = w_{vap} * v, \tag{2.4}$$

where $T_{u/v}$ is moisture transport with subscript referencing the relevant component, w_{vap} is water vapor mixing ratio, and u and v are the zonal and meridional

wind components, respectively. This produced a zonal and meridional moisture transport for each time and height within the combined thermodynamic and kinematic datasets, which were then composited into average meridional and zonal moisture transport.

The final method employed in data analysis was the creation of a scaled velocity. To determine whether or not an enhanced region of moisture transport actually constituted a LLJ or not, the wind velocity components from both Oklahoma and Wisconsin in the summer were scaled against those wind components within the CBL. Areas where wind components maintained a stronger magnitude than the component in the CBL could potentially constitute LLJs. The first step in achieving this was to determine the time and height thresholds for the CBL for both Oklahoma and Wisconsin in the summer. This was done by considering the CBL to be at its strongest when vertical velocity variance (shown in Oklahoma and Wisconsin in the summer in Figure 2.12) was at its greatest. Therefore, a uniform threshold of time and height was established that defined the composite CBL. In Wisconsin, the composite CBL was between 17:00 UTC and 20:00 UTC, and between 250m and 600m AGL. In Oklahoma, the composite CBL was between 18:00 UTC and 21:00 UTC, and between 200m and 800m AGL. For each day, horizontal wind components were averaged within the CBL time-height window. Scaled wind components were then found by dividing the magnitude of individual wind components by that day's CBL wind components, as shown by Equation 2.5:

$$U_{scale} = \frac{u_i}{\bar{U}_{CBL}}, \tag{2.5}$$

where u_{scale} is the scaled velocity, u_i is non-scaled velocity, and u_{CBL} is the daily CBL wind component.

These scaled wind components can be thought of as the ratio between the wind component observation and the daily CBL wind component. Thus, a scaled u-velocity of 3 would mean that observation contained a u wind component 3 times stronger than the CBL u wind. Individual scaled velocity components were then composited for both the Oklahoma and Wisconsin summer datasets.

2.3 Results

2.3.1 Thermodynamic Characteristics

Composite static stability of the ABL from the three datasets are given in Figure 2.7, with composite standard deviations shown in Figure 2.8. This figure begins at a height of 300 meters above ground level (AGL). This is due to the constraints placed upon thermodynamic retrievals. The thermodynamic retrieval method is designed to handle ABLs with standard static stabilities. However, when static stability approaches neutral or superadiabatic, the retrieval method constrains and distributes near-zero static stability within those superadiabatic layers to within the bottom 300 meters AGL. This can cause an issues in thermodynamic profiles in the lowest levels and propagate to data analysis leading to a discontinuity above and below 300 meters AGL in static stability. Data below 300 meters were impacted for all three deployment periods and omitted in both figures.

In all three datasets, a stable layer developed with the onset of nocturnal radiative cooling. The stable layer developed in all three datasets shortly before sunset, with strong near-surface stability lasting until early-to-mid-morning. During the Oklahoma summer deployment, the near-surface stable layer was

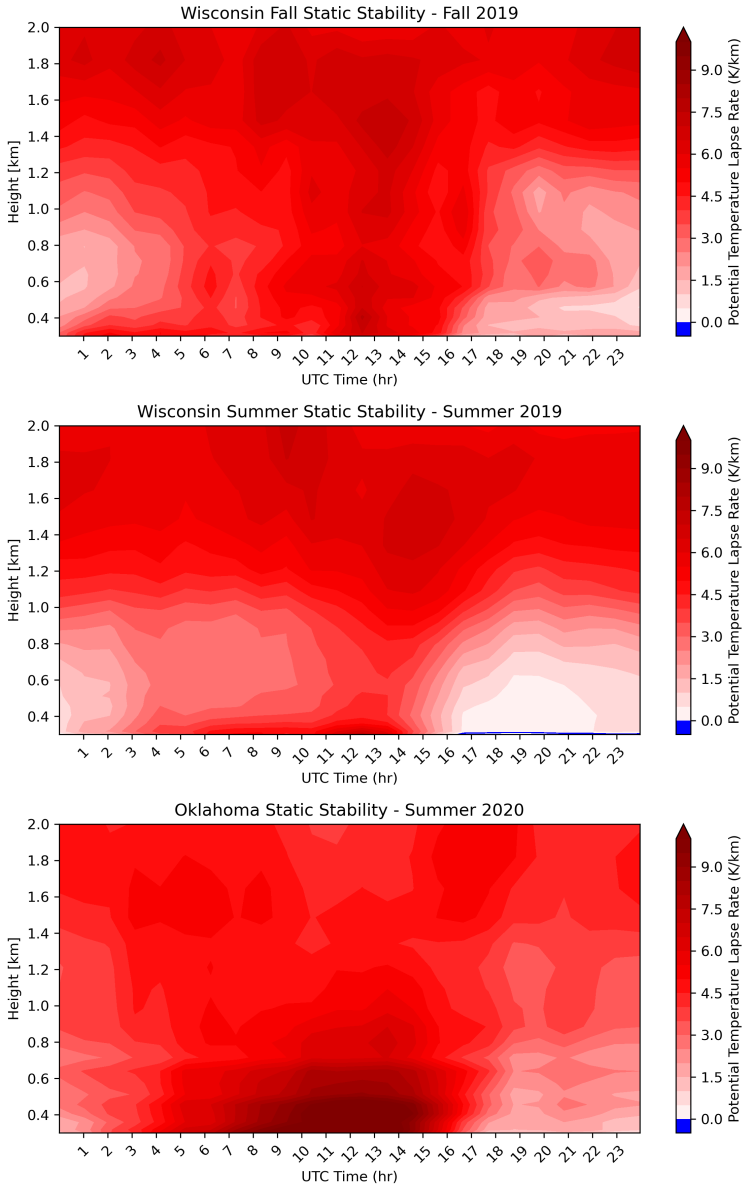

Figure 2.7: Composite mean of static stability from Wisconsin in the fall (top) and summer (middle) as well as Oklahoma in the summer (bottom).

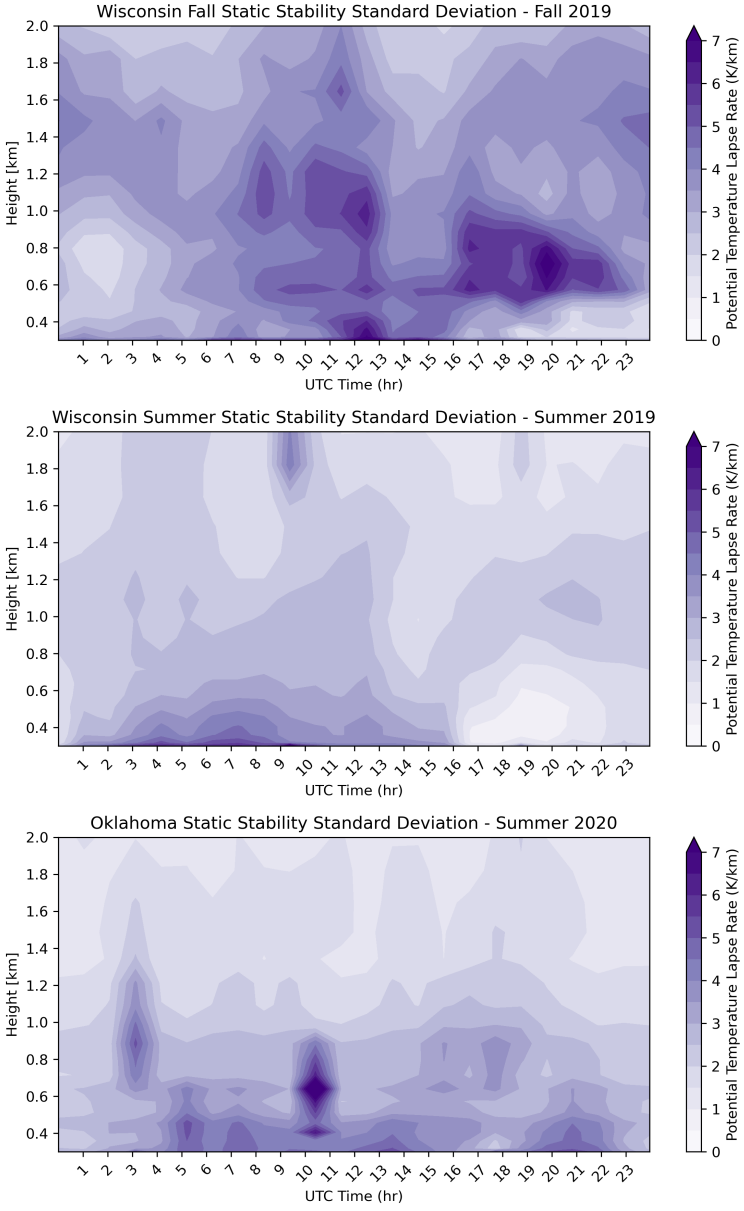

Figure 2.8: Composite standard deviation of static stability from Wisconsin in the fall (top) and summer (middle) as well as Oklahoma in the summer (bottom).

initially shallow in depth early during the evening and continued to deepen with nocturnal cooling. Evidence of the statically stable nocturnal layer at 12:00 UTC could be found as deep as 600 meters in the Oklahoma deployment. By contrast, the depth of the statically stable nocturnal layer in both Wisconsin deployments was much shallower; in fact, evidence of the nocturnal layer only barely reached the 300-meter threshold around daybreak during the summer, and never reached that height AGL during the fall. This is possible evidence of the influence of the treetop canopy—in the more open-terrain Oklahoma deployment location, radiative cooling was much more efficient than in the forested Wisconsin deployment location.

In the canonical ABL outlined in Stull (1988) and shown in Figure 1.1, the residual layer characteristic of the prior day persists above the nocturnal stable layer. Evidence of the residual layer was most prominent in Wisconsin deployments; in the summer period, a well-defined layer between 400 and 1,000 meters maintained lower static stability early in the evening while only gradually becoming more stable until daybreak. Evidence of the residual layer also existed in the fall deployment, particularly prior to 09:00 UTC. The composite residual layer in the fall was quite deep, with indication of it extending to 1,200 meters. In the Oklahoma summer deployment, the residual layer was initially most prominent below 850 meters, extending to as low as 300 meters shortly before sunset. However, the nocturnal surface inversion rapidly deepened such that it eroded the residual layer entirely by the middle of the night.

The daytime convectively mixed layer developed in all three datasets, though again the depth of the mixed layer and static stability within the mixed layer varied by location and season. The Wisconsin summer deployment featured a deep, nearly dry neutral environment from 16:00 UTC to 00:00 UTC with a

depth of over 1,000 meters. The fall deployment was similarly deep, with low composite static stability reaching 1,300 meters over the seasonally abbreviated diurnal period from 17:00 UTC to 23:00 UTC. However, the magnitude of static stability was somewhat higher, suggesting the ABL was not as well-mixed on an average day during Wisconsin fall. Analysis of potential temperature anomalies on individual days within the Wisconsin fall deployment period (Figure 2.9) show a frequent presence of a gradient in potential temperature anomalies. Furthermore, the standard deviation of static stability in Wisconsin in the fall (Figure 2.8) was greater than either of the two summer datasets. This is indicative of a weather pattern in Wisconsin in the fall that did not encourage consistent static stability. In the Oklahoma summer deployment, a convectively mixed layer did not develop until 18:00 UTC, and with a depth of only 800 meters. Furthermore, the mixed layer was not as pronounced in magnitude - static stability was notably higher in Oklahoma than in Wisconsin in either summer or fall.

Composite relative humidity from all three datasets are shown in Figure 2.10. In the lower portions of the ABL during the summer, diurnal relative humidity was generally greater in Oklahoma than in Wisconsin. ABL relative humidity was particularly higher in Oklahoma in the near-surface layer extending down to 300 meters. This trend reversed itself above one kilometer, likely signifying the presence of a stronger elevated mixed layer in Oklahoma than in Wisconsin in the summer. Conversely, relative humidity in the lowest portion of the atmosphere was greater in Wisconsin in the fall.

A combination of composite thermodynamic characteristics is shown in Figure 2.11, which is a profile of the Wisconsin and Oklahoma summer ABLs during the peak of the convective boundary layer. In Oklahoma, a sharper decrease

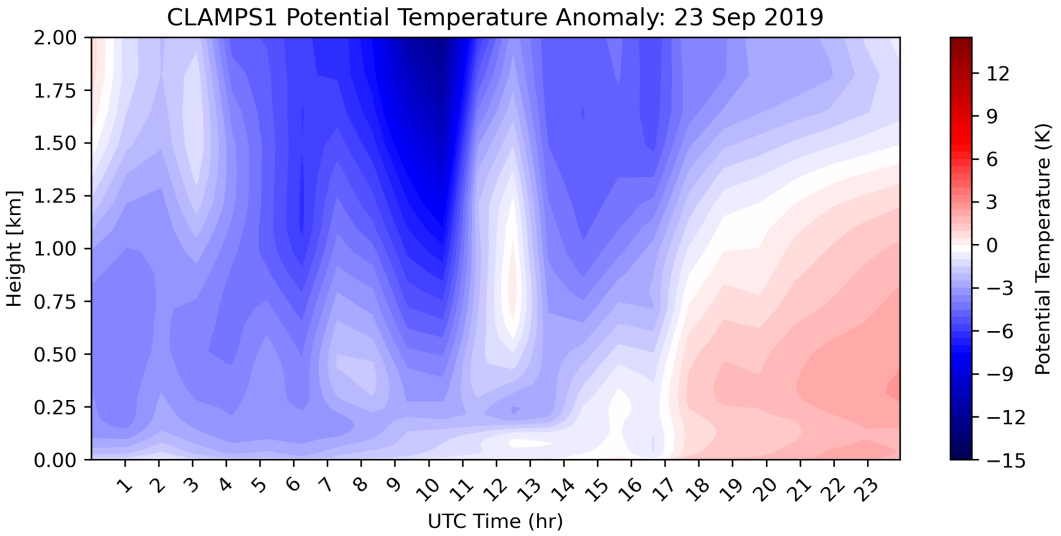

Figure 2.9: Potential temperature anomaly from CLAMPS in the Wisconsin fall dataset on 23 September 2019. The gradient in potential temperature anomalies with height, particularly during the afternoon, shows that static stability within the CBL was not constant day-to-day.

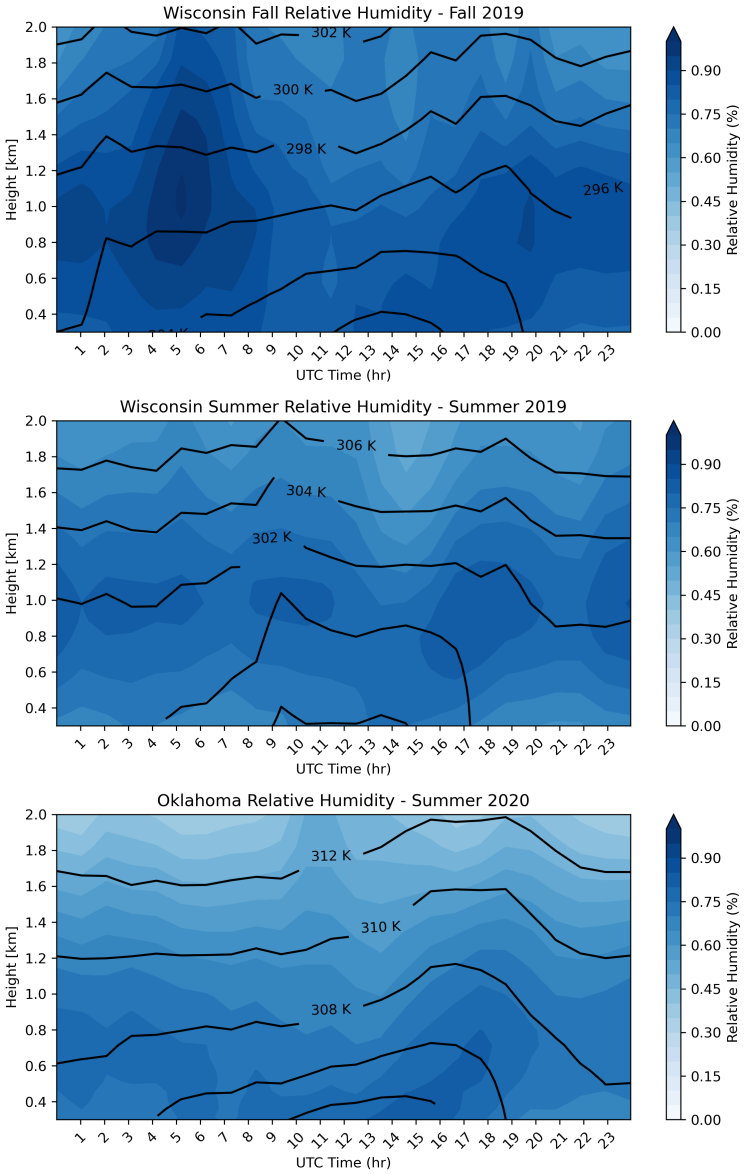

Figure 2.10: Composite daily relative humidity from Wisconsin in the summer (top), Oklahoma in the summer (middle), and Wisconsin in the fall (bottom) in the ABL.

in potential temperature relative to surface potential temperature can be found near the surface than in Wisconsin. However, this is below the 300 meter mark where static stability data were noted as unreliable, and potentially reliant on the optimal estimation retrieval's prior for each location, which is a profile climatology from nearby NWS radiosondes. This climatological prior could have masked actual surface-layer features by instead showing features "normal" to the location that may not have been true during the actual deployments. What is more certain from a comparison of composite profiles, though, is that while lapse rates were stronger within the less-stable Wisconsin boundary layer, dewpoint also decreased more rapidly with height. This suggests more well-mixed boundary layer moisture in Wisconsin relative to the Oklahoma dataset, which mixed-out moisture less efficiently during the peak of the CBL.

2.3.2 Turbulence Assessment

Analysis of Doppler lidar data collected by CLAMPS1 during the fall 2019 portion of the CHEESEHEAD campaign suggests that the vertical extent of lidar observations were limited, impacting data quality within upper portions of the ABL. Thus, the Wisconsin fall composite vertical velocity variance was not included in this study. Composite vertical velocity variance from both summer datasets are provided in Figure 2.12. Both datasets show a general pattern—higher turbulence within periods where the ABL was characterized by the diurnal mixed layer.

In contrast to the thermodynamic structure of the ABL outlined in the previous section, the Oklahoma summer ABL featured both stronger and deeper vertical velocity variance. Turbulence—as represented by this proxy—increased

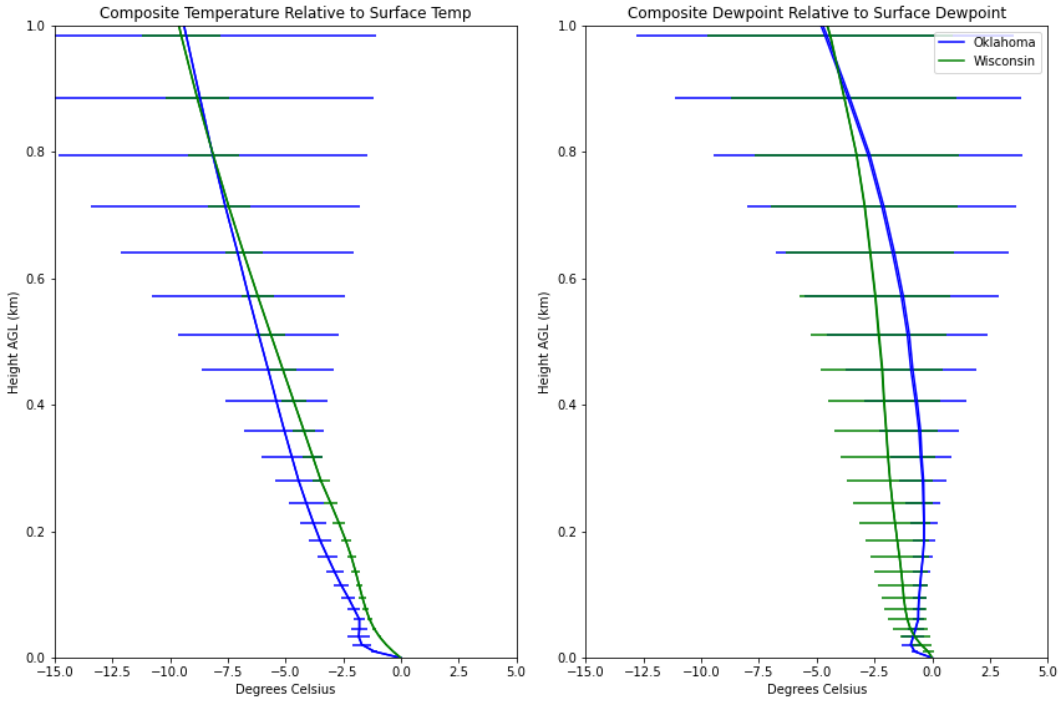

Figure 2.11: Composite profiles of temperature (left) and dewpoint (right) relative to the surface value from the summer datasets in Oklahoma (blue) and Wisconsin (green).

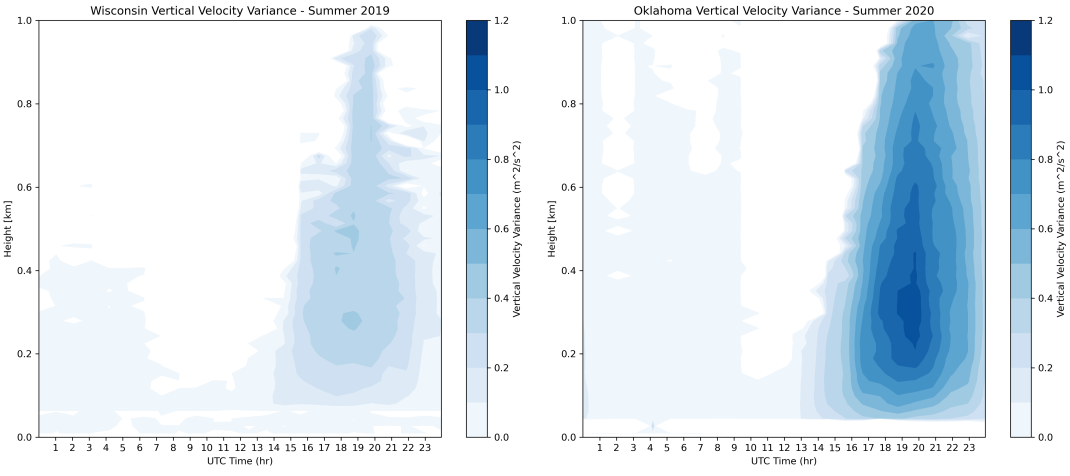

Figure 2.12: Composite mean of ABL vertical velocity variance from Wisconsin (left) and Oklahoma (right) in the summer.

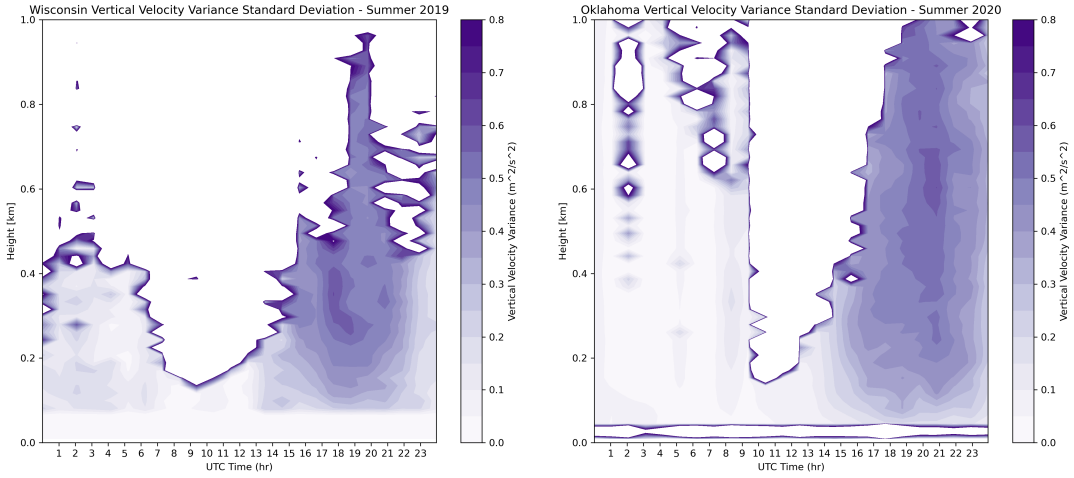

Figure 2.13: Composite standard deviation of ABL vertical velocity variance from Wisconsin (left) and Oklahoma (right) in the summer.

near the surface about 2.5 hours after sunrise (around 14:00 UTC), as the daytime ABL began to develop. Vertical velocity variance increased within the ABL on average throughout the morning and early afternoon, peaking in the 300-600 m layer between 18:00 UTC and 20:00 UTC. Evidence of turbulence could be found as high as 1,000 m after 18:00 UTC. Vertical velocity variance began to drop off in the ABL after 21:00 UTC. Notably, the decrease in ABL vertical velocity variance was much more uniform with height than the increase prior to the peak. Most evidence of turbulence within the ABL was gone by 00:00 UTC, although until about 08:00 UTC a weak vertical velocity variance signal existed within the residual layer up to 600 meters.

The summer ABL in Wisconsin also displayed vertical velocity characteristics that were unlike the anticipated deep, well-mixed structure outlined by thermodynamic assessment. Here, vertical velocity variance was comparatively weak in magnitude. Development of ABL turbulence began near 15:00 UTC between 100 and 300 meters in depth. Moderate composite vertical velocity

variance was noted between 300 and 400 meters near midday, peaking around 18:00 UTC. The highest signal for turbulence was noted around 750 meters from 19:00 UTC to 21:00 UTC, after the peak further below. Whereas the Oklahoma deployment saw a rather abrupt drop-off of ABL turbulence from late afternoon to early evening, composite vertical velocity variance in Wisconsin began dropping from early-to-mid-afternoon, with most of the signal also disappearing by about 00:00 UTC. Similarly to the Oklahoma deployment, there was a small signal for vertical velocity variance in the near-to-just-above-surface layer after sunset in Wisconsin, although this was much more confined to the lower 300 meters of the atmosphere. This weak turbulent signal continued until daybreak and the return of the diurnal ABL. Since the weak turbulence in both Wisconsin and Oklahoma extended to near the surface, within the stable nocturnal layer, this suggests that weak nocturnal turbulence was mechanically generated rather than a product of convection in the residual layer.

2.3.3 Moisture Transport and Scaled Velocity

Figure 2.14 depicts ABL moisture transport in both the u (zonal) and v (meridional) directions from the Oklahoma and Wisconsin summer datasets. There were similarities in the timing of peaks in average daily moisture transport, but also key differences in how that transport was achieved.

In Oklahoma during the summer, the relative minimum in moisture transport in both the zonal and meridional directions occurred during the daytime. In the near-surface layer up to about 400 m, composite meridional moisture transport was negligible around 17:00 UTC. Zonal moisture transport experienced a corresponding minimum in the near-surface layer from 14:00 UTC to 19:00 UTC and the upper ABL from 13:00 UTC to 20:00 UTC. Meridional

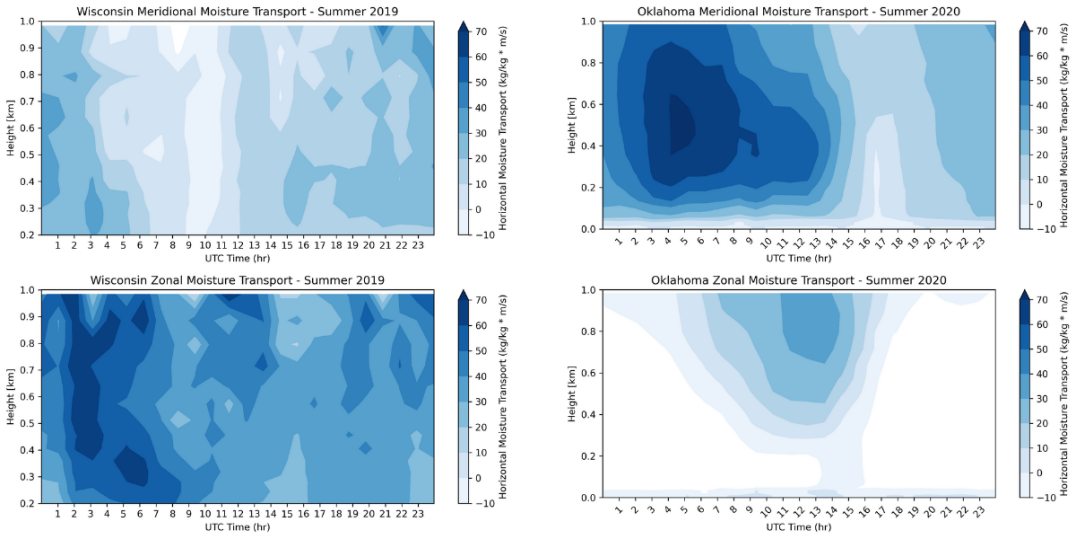

Figure 2.14: Composite meridional (top) and zonal (bottom) moisture transport from Wisconsin (left) and Oklahoma (right).

moisture transport increased in a fairly uniform fashion in the Oklahoma ABL during the afternoon, while zonal moisture transport increased nonuniformly, with the largest afternoon increase occurring between 500 and 800 m. Shortly after 00:00 UTC, moisture transport in Oklahoma increased dramatically. The largest increase occurred in the meridional direction, with strong southerly flow above 100 m contributing to poleward moisture transport. The absolute peak of this meridional moisture flow was between 400 and 600 m, or above the nocturnal surface layer, between 04:00 and 05:00 UTC. Zonal moisture transport increased above 100 m overnight as well, but less dramatically. The peak in zonal moisture transport in Oklahoma in the summer occurred shortly before daybreak, from 10:00 UTC to 12:00 UTC, between 500 and 700 m in height.

Moisture transport in the summer in Wisconsin, by contrast, did not experience peaks in both directions as obviously as in Oklahoma. In fact, the mean meridional wind in the summer dataset in Wisconsin was near-zero, tending

toward slightly negative. Therefore, the mean composite meridional moisture transport was near-zero across the dataset. The mean zonal wind remained out of the west in the entire ABL, providing an opportunity for eastward zonal transport of moisture. The relative minimum in zonal moisture transport in Wisconsin, similar to Oklahoma, occurred during the late morning hours, between 14:00 and 17:00 UTC, particularly above 800 m. While there was little to no afternoon pattern in the increase or decrease of zonal moisture transport in Wisconsin below 600 m, moisture transport increased notably above 600 m during the afternoon hours. The peak in zonal moisture transport at the Wisconsin summer deployment site occurred from about 02:00 UTC to 06:00 UTC throughout nearly the entire 200-1,000 m layer. The magnitude of the peak in zonal moisture transport was similar to the peak in meridional moisture transport in Oklahoma. While zonal transport decreased below 600 m toward sunrise, it was slower to decrease in the upper ABL.

Scaled velocity components from the two summer datasets are given in Figure 2.15. The greatest magnitude of scaled velocities within the two datasets came in Oklahoma, where the meridional wind reached about 4-5 times greater than the average CBL wind at about 05:00 UTC at 700 meters. This elevated area of meridional winds developed shortly after 00:00 UTC and continued throughout the evening until dissipating around 15:00 UTC. A similar maximum in zonal winds was noted in Oklahoma overnight. This maximum peaked later in the evening, between 08:00 UTC and 15:00 UTC, and was somewhat weaker - the scaled velocities were about 3-4 times as strong as the velocities within the CBL. In Wisconsin, scaled zonal velocities were much lower than they were in Oklahoma. At no point in the day and at no height did scaled velocities exceed 2.5 times the zonal wind within the CBL. However, during

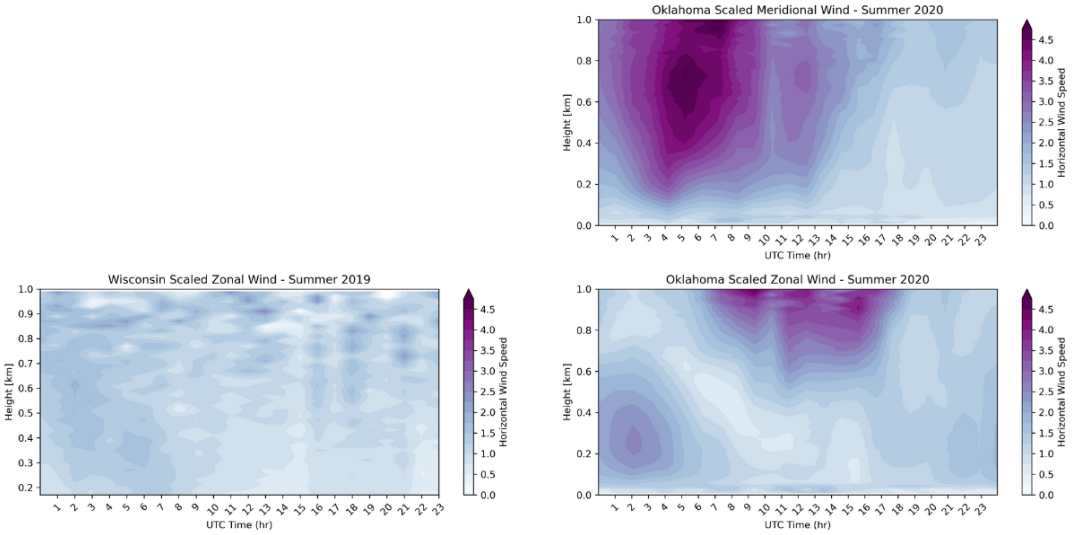

Figure 2.15: Composite mean of scaled velocity components from the two summer datasets, Wiscosin (left) and Oklahoma (right). This shows the three possible wind components across the two datasets that may have contained LLJs.

the period early in the evening that was noted while analyzing zonal moisture transport, there was a notable increase in scaled zonal velocities to about 1.5-2 times as strong as zonal winds within the CBL.

2.4 Discussion

2.4.1 Relationship Between Static Stability and Turbulence

The canonical ABL, as discussed in the introduction and shown in Figure 1.1 from Stull (1988), pairs low static stability with high turbulence during the daytime convective ABL, relatively low static stability with decreased turbulence in the residual layer, and high static stability with near-zero turbulence in the nocturnal stable layer. The three datasets discussed above showed the coupling of mean vertical velocity variance and static stability to be more conditional.

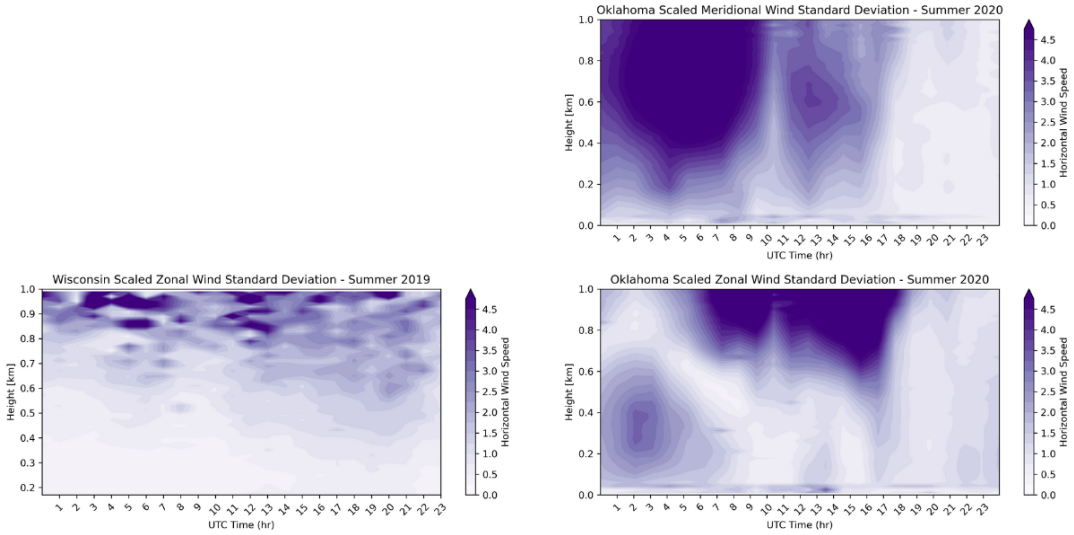

Figure 2.16: Composite standard deviation of scaled velocity components from the two summer datasets, Wiscosin (left) and Oklahoma (right). This shows the three possible wind components across the two datasets that may have contained LLJs.

For example, the Wisconsin summer dataset displayed near-zero static stability within the lower ABL for a substantial portion of the afternoon, indicating deep convective mixing. The Oklahoma summer dataset was more statically stable at similar times and heights above ground level. This suggests that Oklahoma ABL lapse rates were not dry adiabatic every day during the deployment period. It would thus be reasonable to expect greater mean vertical velocity variance to indicate more vigorous mixing in Wisconsin than in Oklahoma. However, Figure 2.12 shows that vertical velocity variance was greater in the more-stable Oklahoma environment than the less-stable Wisconsin environment.

There are several possible explanations for this counter-intuitive negative correlation between ABL static stability and vertical velocity variance. The first explanation stems from the design of the research study. Vertical velocity

variance only maintains an adequate signal-to-noise ratio within the portions of the atmosphere that have sufficient aerosol concentrations for adequate Doppler lidar returns. The Lenschow et al. (1980, 2012) filtering method removed overly noisy data points from the dataset entirely before taking composite means across time of day and height. It would stand to reason, then, that if the ABL depth in Oklahoma was decreased by mesoscale or synoptic-scale factors such as rainfall that increased 500-1000 m AGL static stability on certain days within the deployment period, that mean static stability across three weeks would be greater in Oklahoma than in Wisconsin, while those data points would be removed from the composite vertical velocity variance calculation due to the noisiness of lidar data in rainy conditions. Analysis of surface observations in central Oklahoma during July of 2020 showed negligible rainfall amounts during the afternoon that would have influenced ABL evolution. Furthermore, high temperatures reached 90 degrees every day but one during the deployment period, suggesting that more canonical convective ABLs would have developed every day without being interfered with by weather patterns such as fronts. Therefore, meso- or synoptic-scale phenomena increasing static stability in central Oklahoma can be discounted as a potential explanation for the negative correlation between static stability and vertical velocity variance.

Another possible explanation for the greater turbulence in Oklahoma than Wisconsin was the presence of mechanical turbulence. In environments with stronger horizontal wind speeds, vertical velocity variance would receive a contribution via mechanical turbulence. To account for this, vertical velocity variance was scaled by average daily CBL horizontal winds similar to the method employed to scale horizontal velocity components. The results of this scaled vertical velocity variance field are shown in Figure 2.17. Even after scaling,

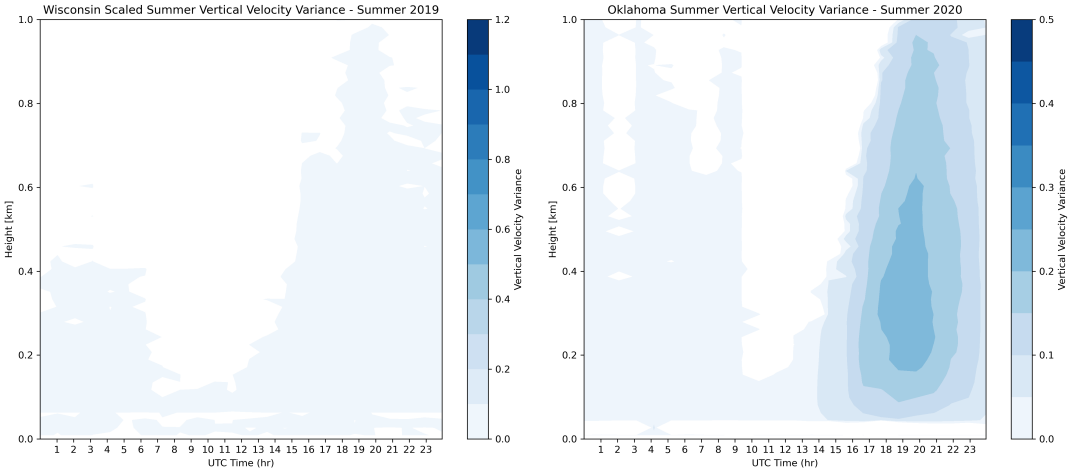

Figure 2.17: Composite ABL vertical velocity variance from Wisconsin (left) and Oklahoma (right) in the summer, scaled by daily mean horizontal winds within the CBL.

peak composite vertical velocity variance was about twice as strong in Oklahoma as it was in Wisconsin. Thus, some other consideration must have led the more-stable Oklahoma ABL to more turbulent than the less-stable Wisconsin ABL.

It is more likely that the negative correlation between static stability and vertical velocity variance is a real feature linked to the atmospheric moisture content at each summer deployment location. As Figure 2.10 indicated, relative humidity was greater during the afternoon across all heights in Oklahoma than it was in Wisconsin. In Figure 2.11, the differences in moisture within the two summer datasets became more pronounced: in Wisconsin, moisture decreased with height steadily throughout the ABL, suggesting that moisture was mixing out as a result of thermals within the unstable ABL. In Oklahoma, moisture was constant or increased with height within the lowest few hundred meters of

the atmosphere before beginning to decrease more uniformly with height in the upper ABL.

These differences may be explained by the background climatic state of each site during their deployment periods. July 2019 in Wisconsin was dry; a U.S. Drought Monitor outlook on 16 July 2019 (Figure 2.18) included an "abnormally dry" designation over the northern part of the CHEESEHEAD domain. Given that Wisconsin is far from a tropical moisture source and that rainfall during the period was sparse, a pattern favoring drier soil conditions and a drier ABL was favored in Wisconsin. It is plausible that the increase in static stability found from summer to fall in Wisconsin was due to a decrease in sensible heating from dry soils. A U.S. Drought Monitor outlook from 24 September 2019 (Figure 2.18), during the fall Wisconsin deployment period, showed that the abnormally dry designation had been removed. It is possible that this in addition to the meso-and synoptic scale impacts analyzed on a day-to-day basis in fall 2019 acted to increase CBL static stability relative to Wisconsin in the summer of 2019.

July 2020 in Oklahoma followed a wet period; heavy rainfall occurred during the late spring that increased soil moisture across the region. Furthermore, July 2020 was quite active tropically. Repeated tropical cyclones in the Gulf of Mexico were fueled by a warm, moist airmass in place over much of the Gulf Coast and south central United States. Oklahoma was within this tropical airmass for much of the studied period, as the composite surface dewpoint (around 72 degrees Fahrenheit) showed.

Because convective mixing occurred in a more humid environment in Oklahoma than in Wisconsin, it is likely that ABL lapse rates were lower as they tended more toward moist adiabatic in Oklahoma. As buoyant surface-based

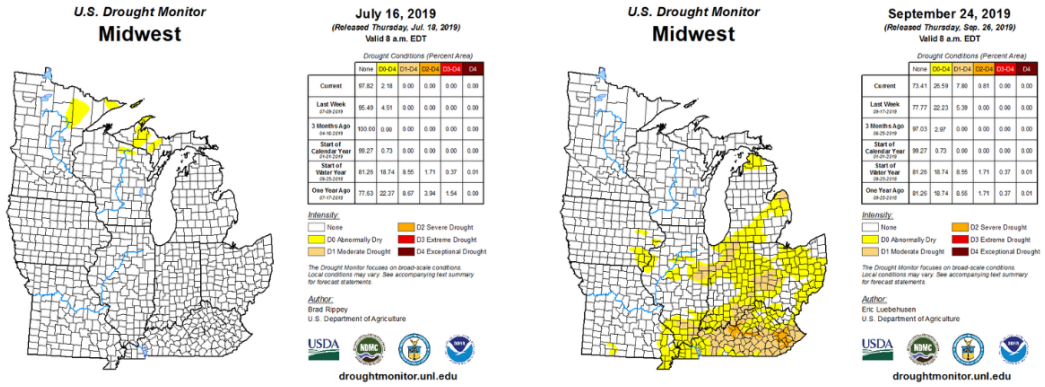

Figure 2.18: U.S. Drought Monitor maps from 16 July 2019 (left) during the middle of the Wisconsin summer dataset and from 24 September 2019 (right), during the middle of the Wisconsin fall dataset (U.S. Drought monitor accessed from: https://droughtmonitor.unl.edu.)

parcels of air in Oklahoma rose, they would have reached their lifted condensation level earlier due to greater water vapor contents. As those buoyant parcels continued to rise, they would cool at a slower rate with height because excess water vapor would be condensed, releasing latent heat and warming the near-condensed layer. Convective mixing would then distribute some of this warmth throughout the ABL and lower lapse rates in Oklahoma. Analysis of National Weather Service radiosondes launched from Norman, Oklahoma (not shown) show the presence of deep moist adiabatic lapse rates in the ABL at times during the Oklahoma deployment period. The drier Wisconsin ABL tended more toward dry adiabatic, as the AERI data indicate. Although this near-zero static stability allowed for turbulent convection to develop within the ABL during the afternoon in Wisconsin, the lower convective instability associated with a dry boundary layer and higher lifted condensation levels may have reduced vertical

accelerations and turbulence magnitudes within the Wisconsin deployment period. Given high ABL moisture content and related lower lifted condensation levels in Oklahoma, higher static stability during that observed period did not preclude the Oklahoma environment from generating convection through the ABL during the afternoon, as parcels were still able to achieve positive buoyancy despite lower lapse rates. While it is counterintuitive that moist adiabatic "subtropical" convection within the ABL is more turbulent than dry adiabatic "continental" ABL convection, the data show that vertical velocity variance was over twice as strong, on average, in the subtropical Oklahoma environment than in the continental Wisconsin environment.

In essence, this shows that static stability is not fully dependent on just potential temperature, and we must consider the impact of virtual potential temperature on static stability. This is sometimes difficult to achieve within the governing equations of atmospheric motions—O'Gorman and Muller (2010) wrote that "the effective static stability does not explicitly depend on mean humidity, and it cannot be derived by replacing the potential temperature with the equivalent potential temperature in the dynamical equations". However, the results here are strongly suggestive that virtual potential temperature must be considered at least analytically to determine the effect that humidity has on buoyancy and turbulence. Virtual potential temperature is not explicitly calculated here—as Figure 2.9 shows, the uncertainty for both temperature and humidity were high through thermodynamic retrievals. Virtual potential temperature is a product of both temperature and humidity variables, and explicitly calculating a variable as a product of two uncertain variables was not performed for the exacerbating effect it would have on potential error. Instead, the impact of virtual potential temperature was considered analytically as shown above.

2.4.2 Moisture Transport and NLLJ Presence

Previous studies have shown that the Great Plains summer NLLJ originates over the southern Great Plains (Wu and Raman 1998). Initially a southerly jet, the NLLJ tends to veer as it spreads northward, with the result being that the NLLJ spreads north and east of the southern Great Plains later in the evening (Jiang et al. 2007), while the strongest wind components within the NLLJ veers from meridional to zonal over the course of the night. In Oklahoma, much closer to the source region of the NLLJ, the jet intensified shortly after sunset, with meridional moisture transport outweighing zonal moisture transport initially. It is noteworthy that after midnight, scaled meridional winds and meridional moisture transport actually decayed in Oklahoma. Meanwhile, as the meridional jet decayed closer to daybreak, zonal moisture transport and scaled zonal winds reached a relative maximum. Carroll et al. (2019) observed the same veering phenomenon during the Plains Elevated Convection at Night (PECAN) campaign in Kansas, noting that this was related to the inertial oscillation and downslope acceleration. The relationship between the NLLJ and Oklahoma's subtropical high-humidity environment is also clear; the southerly component of the NLLJ that was most prominent between 03:00 UTC and 08:00 UTC during this dataset would have constantly transported moisture northward into central Oklahoma. Much of the mean moisture transport during this deployment period would have been flow from the Gulf of Mexico, although local advection from wetter or drier portions of the Great Plains would also have influenced the mean moisture transport (Smith et al. 2019).

Wisconsin is far from the southern Plains and would not see a southerly jet develop after sunset — Algarra et al. (2019) found that the region that made up the CHEESEHEAD domain was just north of the axis of appreciable moisture

transport by the NLLJ in its sample of five NLLJ studies; however, significant moisture transport did occur into central Wisconsin with the CHEESEHEAD domain in such a position that it would likely encounter a later, weaker, and veered NLLJ. We must look to other forcing mechanisms besides that of the NLLJ to consider the possibility of a zonal LLJ in Wisconsin early in the evening. Northern Wisconsin during the middle of July 2019 was influenced by synoptic-scale factors. A stationary-to-warm-frontal boundary was draped across southern to central Wisconsin for several days, per Weather Prediction Center archived surface analyses. The CHEESEHEAD domain, including the WLEF tower where this deployment was conducted, was north of the frontal boundary. Although on average one would anticipate a mean ABL wind direction from the southwest (per the Wisconsin State Climatology Office averages), the mean ABL wind direction during the portions of nighttime over the last week of July 2019 actually had a slight northerly component. This lends a possible solution to the presence of enhanced zonal winds early in the evening. It is possible that a low-level jet developed within the frontal zone early in the evening that was largely westerly over Wisconsin. Over the course of the night, it veered toward northwesterly, explaining the "minimum" in northward moisture transport later in the evening, as well as the decrease in magnitude of zonal moisture transport. This could have been present on some or all of the days that the frontal zone was present in north central Wisconsin during July of 2019. Without higher-resolution profiling systems in place operationally in the United States, it is hard to establish conclusively whether that was happening synoptically. What is certain is that some sort of zonal LLJ, probably not related to the NLLJ, was present in Wisconsin during the summer of 2019.

2.5 Conclusion

High-quality, long-duration remote sensing platforms allow for a new opportunity to explore heterogeneities in ABL evolution across climatic regimes and seasons. Datasets collected by the CLAMPS and SPARC observational platforms were analyzed for that purpose. Given the presence of both thermodynamic and kinematic profilers on these platforms, a comparison of thermodynamic structure and turbulence within the ABL was possible. Three datasets were considered: in northern Wisconsin in the fall; the same region in the summer; and Oklahoma in the summer. In Wisconsin, ABL static stability was lower in the summer than in the fall, corresponding to a more canonical ABL. In Oklahoma in the summer, static stability in the ABL was greater during peak daytime heating than in Wisconsin in the summer. Counterintuitively, vertical velocity variance was greater in Oklahoma in the summer during peak daytime heating than Wisconsin. This suggests that the relationship between ABL mixing and strength of turbulence is not always a direct correlation. The same thermodynamic and kinematic datasets allow for a comparison of moisture transport across different locations. In Oklahoma in the summer, meridional moisture transport peaked early overnight with the intensification of the NLLJ. While meridional moisture transport gradually declined overnight, zonal moisture transport peaked shortly before sunrise as the NLLJ veered over the Southern Plains. In Wisconsin in the summer, no meridional component of the NLLJ could be detected. However, there was a peak in zonal moisture transport early in the evening, providing evidence of a LLJ in place during the studied period of summer 2019 in Wisconsin.

Uncertainty is introduced into the results via confounding meteorological variables. Were the Wisconsin summer deployment not generally north of a quasi-stationary frontal zone, there may have been a stronger mean meridional influence from the NLLJ. Oklahoma frequently experiences summer droughts; in a year in which the land surface was drier, it may not have been possible to make the distinction between turbulence in a subtropical environment and turbulence in a continental environment. Furthermore, the length of the deployment periods, from just over a week for the Wisconsin summer lidar data to several weeks for Oklahoma summer data, give only a range of 8 to 18 24-hour ABL cycles to analyze. These results cannot be treated as representing climatological ABL evolution for the locations and seasons involved. The results do provide an example of the usefulness of comparison of remote sensing datasets to understand ABL evolution, as well as providing a challenge to the typically understood relationship between the magnitude of turbulence and static stability within the ABL. Further deployments of observational platforms such as CLAMPS will provide more opportunities for intercomparison of ABL evolution across season, climate regime, land cover regime, and topography.

Chapter 3

WoFS Verification

3.1 Introduction

3.1.1 WoFS Verification Motivation

Experimental WoFS data are publicly available from real-time runs beginning in April of 2018. This means that WoFS now has a track record that scientists at NSSL are able to evaluate. Over the past five severe weather seasons, the model has been run over 200 times coinciding with greater-than-climatological-norm risks for impactful convection. As NSSL plans on transitioning WoFS from experimental toward operational use by forecasters, there is a need for scientists working at the intersection between research and operations to aid in forecaster understanding of the utility of WoFS. The model's half-hourly runs and the plethora of available output mean that operational forecasters can easily be overwhelmed by details; an effective research-to-operations transition will help highlight which WoFS products are most and least useful for forecasters to lean upon in different convection regimes or regions. The 19-20 July 2019 event provides an ideal opportunity for WoFS evaluation for two primary reasons: there were multiple identifiable regimes of severe weather within the event that can be individually verified, and the location of the severe weather event

means that CHEESEHEAD profilers were impacted, allowing for a comparison of WoFS forecasts to observed profiles that are not typically available.

3.1.2 Event Summary

The 19-20 July 2019 severe weather outbreak occurred over a long duration as multiple waves of convection impacted the upper Midwest. On 19 July, the Storm Prediction Center outlined a heightened risk for severe weather across parts of eastern Minnesota and northern Wisconsin. The environment was characterized by extremely high convective instability and sufficient deep-layer shear for potentially tornadic supercells to develop. Eventually, upscale growth into a mesoscale convection system (MCS) was anticipated, with a risk for damaging wind gusts along the gust front. For this study, there will be three primary convective regimes evaluated. National Weather Service radar data from the first two regimes are shown in Figure 3.1 . The first regime was a supercell that developed ahead of the primary convective line across northern Wisconsin. This supercell produced two EF-0 tornadoes (Figure 3.2) before being overtaken by the primary convective line, which had a faster east-southeastward motion than the supercell. As the MCS overtook the supercell, the supercell was absorbed into the northern end of the MCS with a cyclonic bookend vortex noted on radar reflectivity. This bookend vortex produced by the merger between the supercell and MCS comprises the second convection regime studied in this work. The bookend vortex produced an enhanced region of significant (80-110 mph) straight-line wind damage across north central Wisconsin southeast of the town of Rhinelander (Figure 3.2), while the entire length of the MCS south of the bookend vortex produced a long-duration swath of damaging wind reports across Wisconsin over the evening. Following these two regimes, the

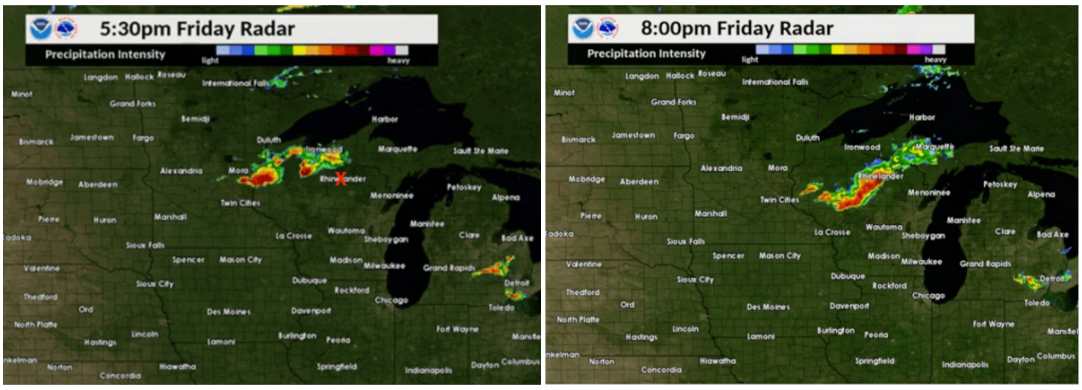

Figure 3.1: Radar images from The National Weather Service La Crosse office, showing the development of the supercell in regime 1 west of Rhinelander (left) before it was overtaken by the MCS in regime 2 near Rhinelander (right). Rhinelander is denoted by the red X on the left panel.

outflow from the MCS traveled south across Wisconsin overnight before stalling and retreating northward into central Wisconsin early in the morning of 20 July. Along this outflow boundary, new convection developed in the third regime during the morning of 20 July (Figure 3.3). This new convection organized itself into an MCS with an embedded supercell latching onto the outflow boundary and producing several tornadoes in rapid succession.

To better understand how well WoFS handled the mesoscale environment over the course of the 19-20 July 2019 event, WoFS was run ex post facto with hourly runs continuing until an initialization time of 14:00 UTC on 20 July 2019, over a domain including much of the Upper Midwest. This allowed researchers to not just focus in on the first two convection regimes that the real-time WoFS run covered, but to allow for analysis of the outflow boundary's motion over the night of 19-20 July leading up to the MCS within the third convection regime during the morning of 20 July.

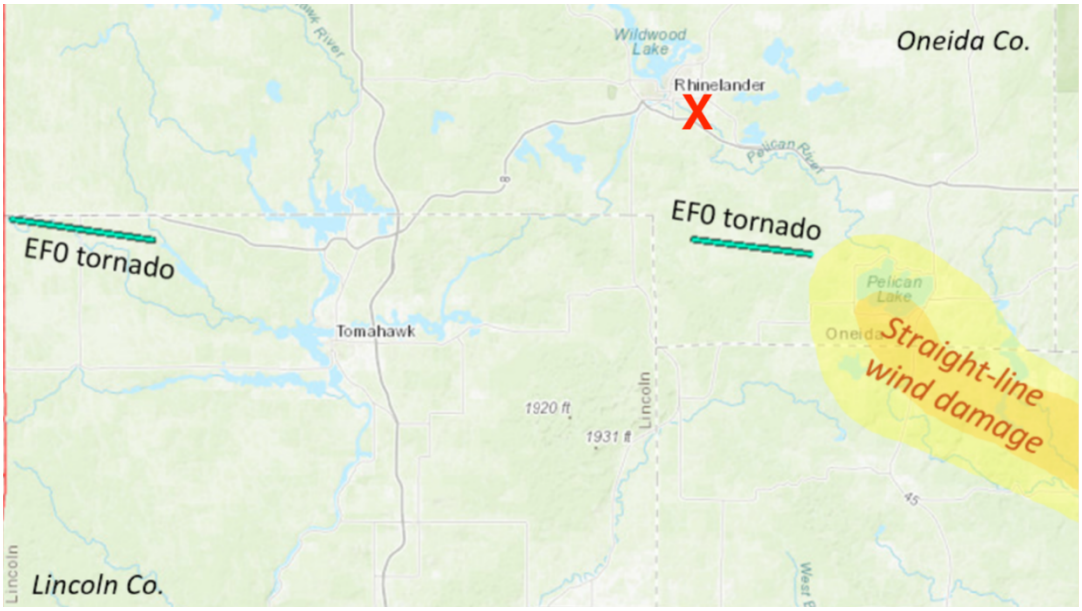

Figure 3.2: Zoomed in map showing the track of the two EF-0 tornadoes produced by the supercell south and west of Rhinelander, as well as the swath of straight-line winds that occurred during the supercell-MCS merger blowdown. Rhinelander is denoted by the red X.

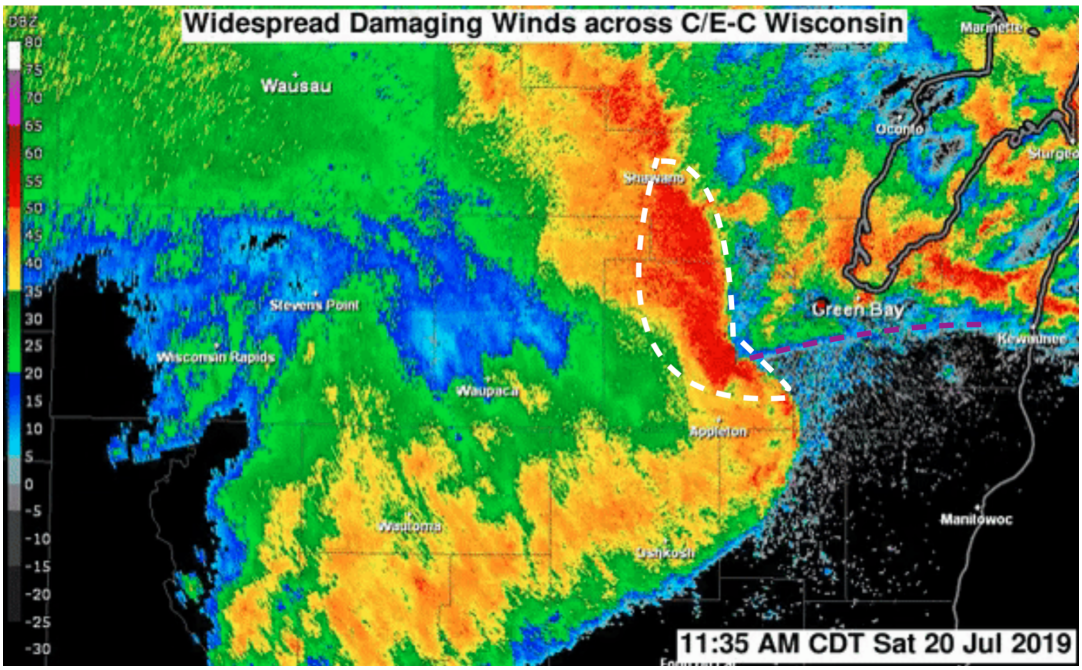

Figure 3.3: Radar image from National Weather Service Green Bay showing convection evolving along an outflow boundary (purple) just south of Green Bay, Wisconsin. The embedded supercell north of Appleton (white) was the source of several weak tornadoes in rapid succession.

3.2 Data and Methods

3.2.1 Wind Profile Comparison

The weakly tornadic supercell within the first convection regime passed across the CHEESEHEAD domain around 00:00 UTC on 20 July 2019. This provides an opportunity to compare pre-convective WoFS zero-hour forecasted profiles to observed wind profiles at the site of a radar wind profiler in Prentice, Wisconsin during the afternoon of 19 July. Located at this site was a NOAA Physical Sciences Laboratory (PSL) 915 MHz wind profiler. The profiler is a Doppler radar that operates at a slightly off-vertical angle to generate wind profiles above a fixed location (Wilczak and Gottas 2020). Data were averaged over the course of 55 minutes to create a profile for a given hour. Two different sets of profiles were available from Prentice every hour — a high-resolution dataset with a vertical resolution of 55 m up to a height of 2.6 km, and a low-resolution dataset with a vertical resolution of 97 meters up to a height of 6.8 km.

The wind profiles collected at Prentice were compared to forecast wind profiles generated at the nearest WoFS grid point on the afternoon of 19 July. Comparisons were made at 21:00, 22:00, and 23:00 UTC. At 00:00 UTC on 20 July, Doppler radar archives show that Prentice was in the rear flank downdraft (RFD) region of the supercell. Wind profiler data for the 00:00 UTC hour was impacted by the nearby storm, and thus the study of the prestorm environment was cut off at 23:00 UTC. Thus, the comparisons allow for a study of wind profiles in the far-storm environment transitioning into the near-storm inflow with decreasing lead time prior to supercell passage. Wind profiles were compared in two different ways. Vertical profiles of the meridional and zonal components

were compared between WoFS and the high-resolution profiler data to an elevation of 2.5 km AGL. This allowed for a high-resolution comparison of boundary layer wind profiles. Hodographs were then generated comparing 0-6.8 km winds between WoFS and the low-resolution profiles. This allowed for a deeper analysis of how the vertical shear profile would have affected storm morphology on 19 July.

3.2.2 Outflow Boundary Verification

A challenge in verifying WoFS performance in boundary placement is defining the location of both observed and modeled boundaries. Fronts are rarely discrete, one-dimensional lines as depicted on surface maps. Rather, a front is often a zone comprising the strongest gradient in surface thermodynamics. The Weather Prediction Center notes in its educational material that this is particularly true with warm fronts, which commonly have broad frontal zones compared to cold fronts and outflow boundaries. Furthermore, automated frontal depictions must factor in the relative coarseness of available data. While WoFS has three-kilometer gridded data and therefore offers more precision in boundary forecasting, observed surface data are available in a sparser grid and provide less precision. These factors introduce uncertainty into boundary verification efforts that must be accounted for by the verification method.

The outflow boundary over the evening of 19-20 July is the focus of this study. This boundary was identified using a fuzzy logic method developed for this application. The fuzzy logic method identified locations within the observed and modeled domains that triggered each chosen threshold of environmental parameters. The outflow boundary contained a much sharper gradient in dewpoint temperature than the warm front that had been across central Wisconsin earlier

in the day; thus, the outflow boundary logic first passed each gridded data point through a thresholding filter of dewpoint gradient — a lower threshold across a large distance and a higher threshold across a short distance. All data points that maintained sufficient dewpoint gradient magnitudes then passed through the next filter, which was mass convergent. The outflow boundary was convergent, so any areas of divergence or weak convergence were removed from consideration to be an outflow boundary point. These two variables comprised the main filters within the fuzzy logic algorithm. However, the same two variables often provided other boundaries, particularly along the edge of bodies of water. Thus, some specific thresholding was performed to ensure that the actual outflow boundary was the only one that the algorithm depicted as much as possible. These thresholds included a minimum and maximum in dewpoint between 20.5C and 27C, as well as latitude and longitude thresholds. The step-by-step methodology within this fuzzy logic algorithm is shown in a flow chart in Figure 3.4.

Fuzzy logic thresholding was applied uniformly to both observations and WoFS forecasts for the outflow boundary. To identify the observed boundaries, surface meteorological data were used from the National Center for Environmental Information (NCEI). Data were considered for a valid hour if they were collected within 10 minutes of the valid hour in either direction. This allowed for the densest possible network of observations and greater precision in the observed boundary location. WoFS forecast boundaries were found using an ensemble probability method wherein each individual member passed through the fuzzy logic method, with the probability representing the fraction of members identifying the boundary at a location. Boundary error was defined by taking the location of the maximum ensemble boundary probability along each

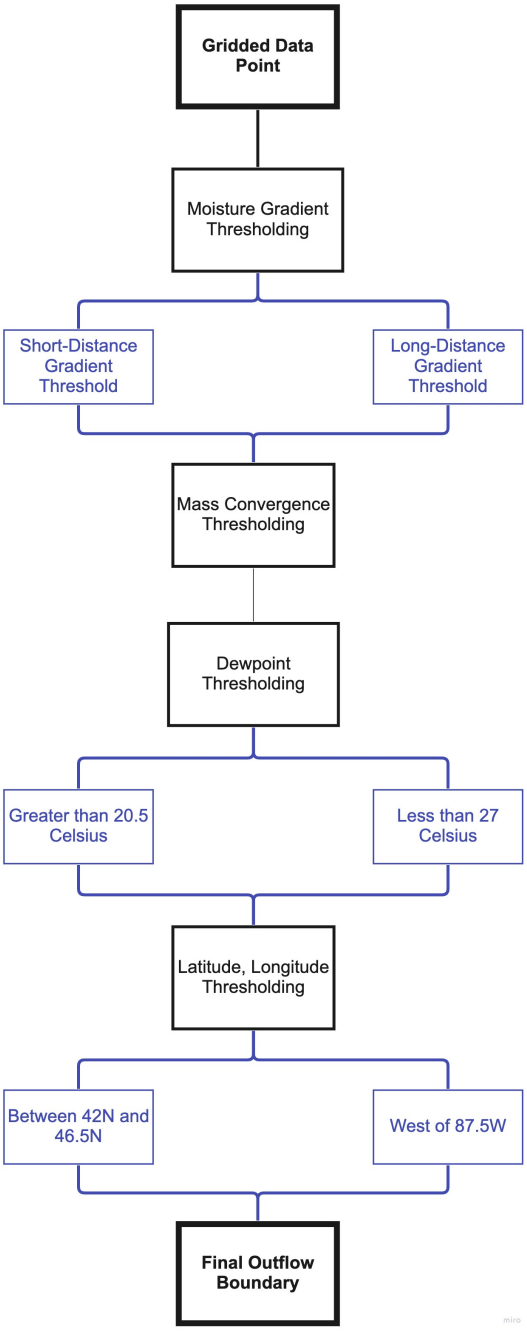

Figure 3.4: A flowchart demonstrating each individual threshold a grid point would need to meet to be considered part of the outflow boundary.

longitudinal grid line and finding the minimum distance to the observed boundary. This boundary error was averaged along each longitudinal grid line from 88.5W to 94W to create a longitudinally-averaged WoFS boundary error.

3.3 Results

3.3.1 Regime 1: Tornadic Supercell

Observed boundary layer wind profiles at Prentice are shown side-by-side with WoFS model zero-hour forecasted profiles in Figures 3.5, 3.6, and 3.7. The general character of observed and forecast profiles were similar. Meridional winds were largely steady with height, around 5 m s^{-1} at 21:00 UTC and increasing to around 10 m s^{-1} at 23:00 UTC. Zonal winds were negative near the surface before becoming positive within the boundary layer and increasing above that. While the general characterization of both forecast and observed profiles were similar, differences in the profiles are evident that potentially influenced convective morphology. At 21:00 UTC, WoFS underestimated the magnitude of negative zonal winds near the surface. While the degree of backing of the zonal wind remained roughly constant near the surface across all three hours, WoFS increased the magnitude of the near-surface negative zonal winds, thus creating a slight overestimate in the magnitude of zonal winds by 23:00 UTC. WoFS also poorly depicted meridional wind shear as the supercell approached. Meridional wind profiles at 21:00 UTC contain the lowest errors of the three compared times between WoFS forecasts and observations. Over time, WoFS increased vertical meridional wind shear, with southerly winds aloft increasing near the top of the boundary layer. However, while southerly winds did increase

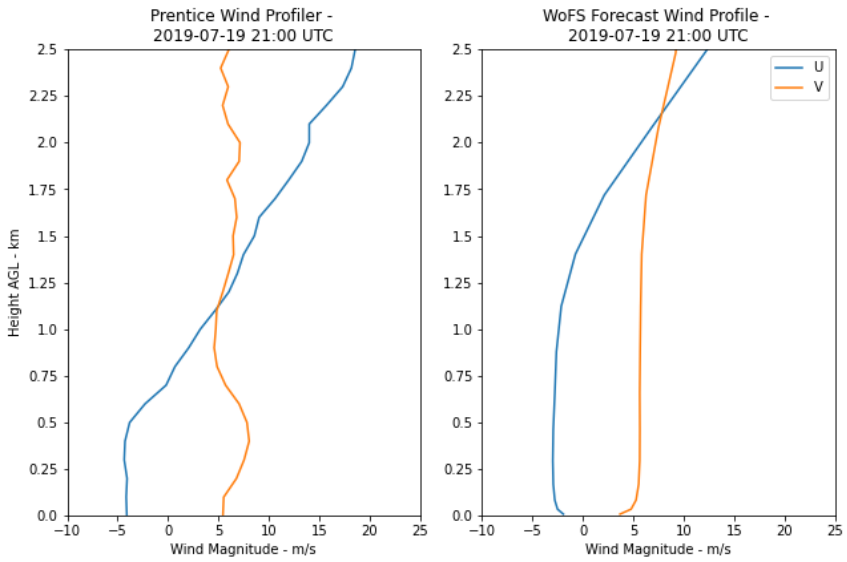

Figure 3.5: Observed (left panel) and WoFS forecasted (right panel) ABL wind profiles at the Prentice wind profiler at 21:00 UTC on 19 July 2019. Zonal winds are shown in blue while meridional winds are shown in orange.

in time via the Prentice profiler, vertical meridional wind shear did not increase to the degree that WoFS zero-hour forecasts showed.

Hodograph comparisons (hodographs are shown in Figures 3.8, 3.9, and 3.10) between WoFS and the Prentice profiler show the impact that the difference between WoFS forecasts and observed profiles had on anticipated storm hazards. WoFS ensemble mean and parameterization mean hodographs are closely in line with both the low-resolution and high-resolution wind profiler at 21:00 UTC. However, by 22:00 UTC all WoFS parameterization members generated a zero-hour forecast hodograph with increasing low-level streamwise vorticity, beginning to resemble a classic "sickle shape". By 23:00 UTC, this was even more pronounced, with WoFS hodographs depicting a low-level shear profile almost perfectly in line with what is understood to be ideal for a tornadic supercell (Weisman and Klemp 1984). In reality, while the Prentice wind profiler

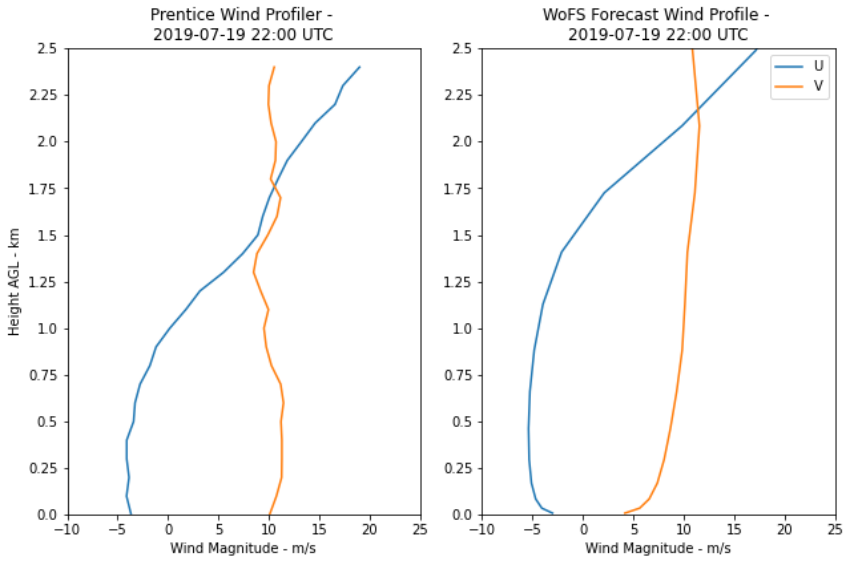

Figure 3.6: Observed (left panel) and WoFS forecasted (right panel) ABL wind profiles at the Prentice wind profiler at 22:00 UTC on 19 July 2019. Zonal winds are shown in blue while meridional winds are shown in orange.

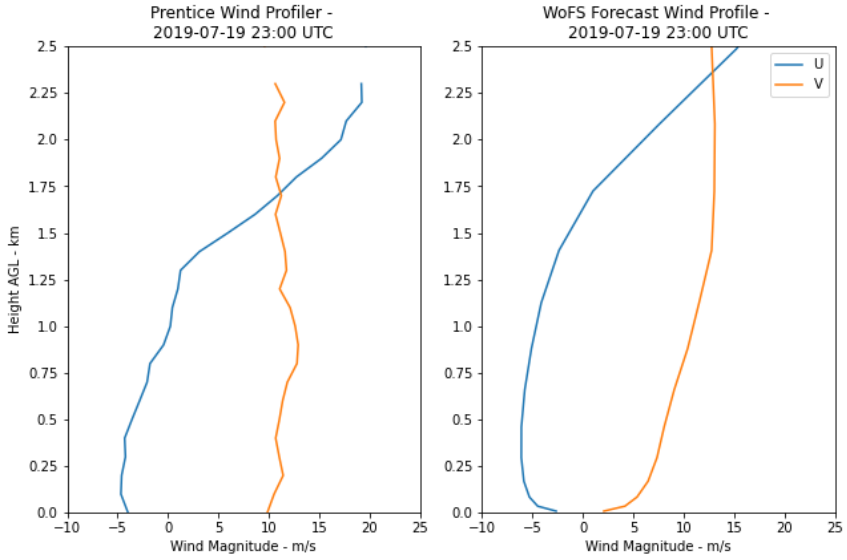

Figure 3.7: Observed (left panel) and WoFS forecasted (right panel) ABL wind profiles at the Prentice wind profiler at 23:00 UTC on 19 July 2019. Zonal winds are shown in blue while meridional winds are shown in orange.

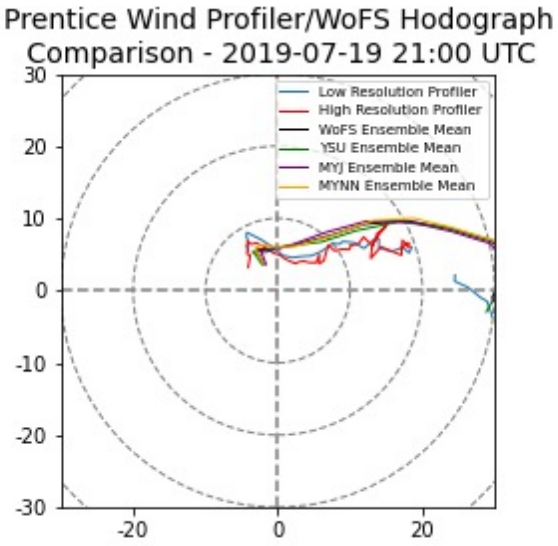

Figure 3.8: Observed and WoFS forecasted hodographs at the Prentice wind profiler at 21:00 UTC on 19 July 2019.

observed a small degree of low-level shear enhancement between 21:00 UTC and 23:00 UTC, shear enhancement did not occur to the same degree that WoFS zero-hour forecasts showed. Prentice profiles suggest adequate low-level and mid-level shear for potentially tornadic supercells, but not as favorable of an environment for long-lived, strong tornadoes as the higher-streamwise-vorticity environment depicted by WoFS. The supercell passed by the Prentice site around 00:00 UTC. Between 23:47 and 00:00 UTC, it produced an EF-0 tornado with peak 75 mph winds estimated by the National Weather Service in Green Bay. The supercell produced another EF-0 with 75 mph estimated winds between 00:49 and 00:58 UTC prior to merging with the MCS. Thus, the storm was only weakly tornadic, an indicator that the weaker-streamwise-vorticity environment observed by the Prentice radar wind profiler was more representative of the near-storm environment.

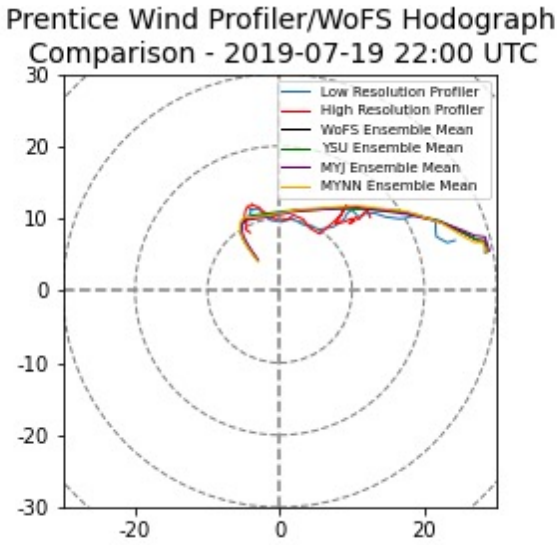

Figure 3.9: Observed and WoFS forecasted hodographs at the Prentice wind profiler at 22:00 UTC on 19 July 2019.

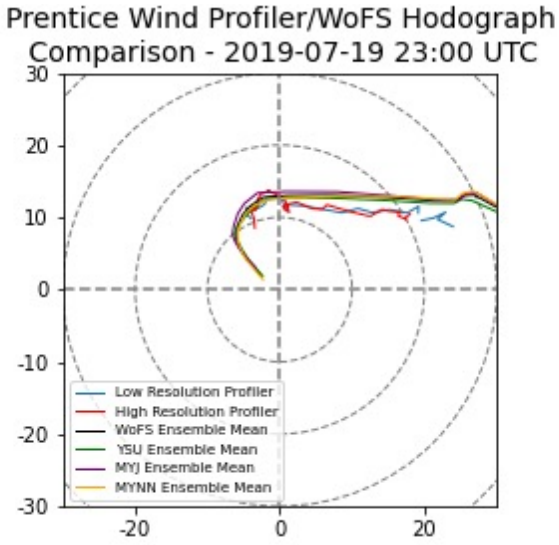

Figure 3.10: Observed and WoFS forecasted hodographs at the Prentice wind profiler at 23:00 UTC on 19 July 2019.

3.3.2 Regime 2: Supercell-MCS Merger

The supercell-MCS merger southeast of the CHEESEHEAD domain near Rhinelander, Wisconsin produced damaging winds even stronger than those estimated within the supercellular tornadoes. WoFS was designed as a tool to aid forecasters in identifying enhanced hazard potential within convection; thus, this blowdown event provides an opportunity to explicitly verify WoFS performance highlighting the potential for significant damaging wind gusts. The 00:00 UTC WoFS run was chosen for this purpose for several reasons. WoFS is intended to highlight short-term hazards with ongoing convection, and with the bookend vortex peaking in strength around 01:30 UTC, an accurate forecast from WoFS would provide around 90 minutes of model lead time. A forecaster would not have a full 90 minutes of lead time in reality, as the 00:00 UTC run would likely not finish running past the relevant time frame until about 00:45 UTC. However, a forecaster could still have valuable lead time from the 00:00 UTC run in time for the model to inform their situational awareness prior to the actual 01:30 UTC peak bookend vortex strength. Furthermore, the 00:00 UTC WoFS run assimilated and depicted the supercell ahead of the northern flank of the MCS in its zero-hour forecast as shown by Figure 3.11. This provided the model with an opportunity to resolve the upcoming merger and bookend vortex.

Figure 3.12 shows 90th ensemble percentile maximum convective wind gusts from the 00:00 UTC WoFS run. In essence, this shows maximum wind gusts from the 2nd or 3rd highest member of the 18 WoFS members, although in outlier scenarios the 90th percentile maximum gust may occur from the highest member. There is an axis of enhanced damaging wind gusts across central Wisconsin as depicted by WoFS; however, the actual blowdown within the bookend vortex as shown in Figure 3.12 actually occurred 1-2 counties north of where

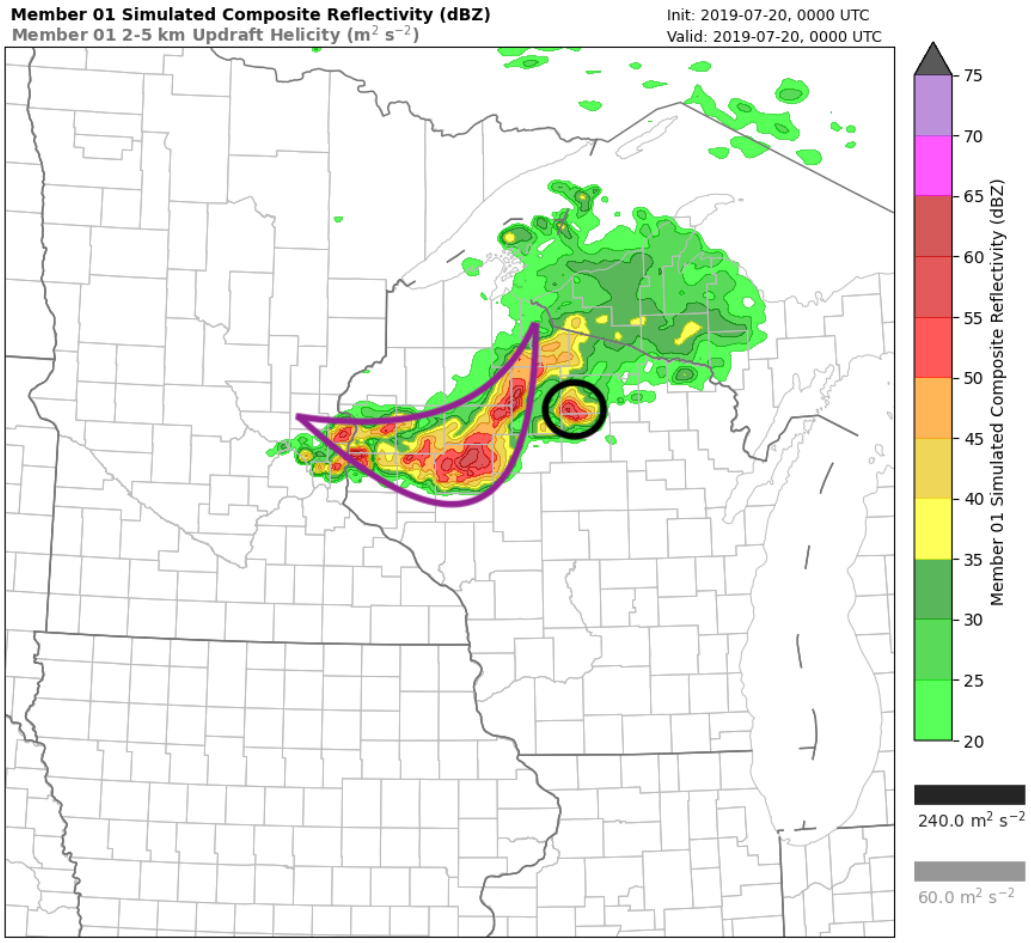

Figure 3.11: A zero-hour forecast at 00:00 UTC of simulated radar reflectivity from WoFS ensemble member 1, which was representative of the ensemble as a whole, showing the supercell (black) east of the developing MCS (purple).

the WoFS swath occurred. This is rather low accuracy for a short-term forecast, with the forecast made even less useful by the absence of any signal for enhanced damaging winds within the supercell-MCS merger region. Analysis of WoFS output suggests that it produced a different convective outcome than reality. In particular, WoFS ensemble members developed a bow echo across the region south of the MCS/supercell merger (Figure 3.13). It is within this bow echo that the 90th percentile WoFS forecasted maximum wind gusts were the greatest across the early evening of 19-20 July 2019. Meanwhile, WoFS ensemble members failed to properly merge the supercell amd MCS. Analysis of radar data from the early evening of 19-20 July shows that a bow echo did develop within the region that WoFS showed; however, damaging wind reports from this region were sporadic, and were mixed with several embedded tornadoes.

3.3.3 Regime 3 - Outflow Boundary

Outflow boundary verification was performed for each of the 14 valid WoFS hours that occurred after passage of the supercell at the Prentice site. At each of those 14 hours, WoFS forecasts were verified from zero-hour analysis to the maximum hour-6 forecast time, meaning that 7 WoFS runs were verified at each valid hour. An example of the WoFS verification process is provided for the 03:00 UTC WoFS run valid at 06:00 UTC, which was representative of the process as a whole. Figure 3.14 shows the observed outflow boundary at 06:00 UTC, the 03:00 UTC WoFS ensemble forecasted outflow boundary valid at 06:00 UTC, and the WoFS error plot. Table 3.1 is an error matrix that denotes longitudinally-averaged outflow boundary location error between 88.5W and 94W for each run of WoFS across each valid hour.

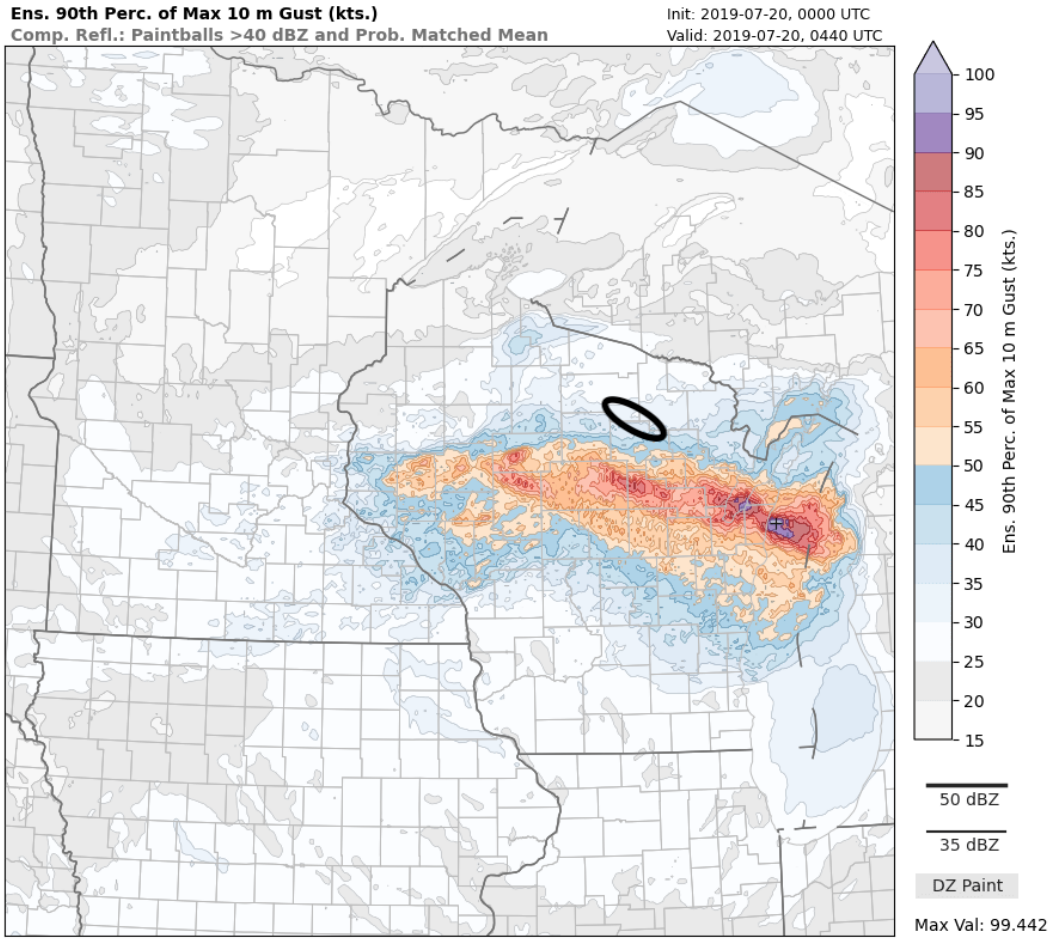

Figure 3.12: WoFS ensemble 90th percentile maximum wind gusts from the 00:00 UTC run. The circled area denotes where the bookend vortex "blowdown" occurred.

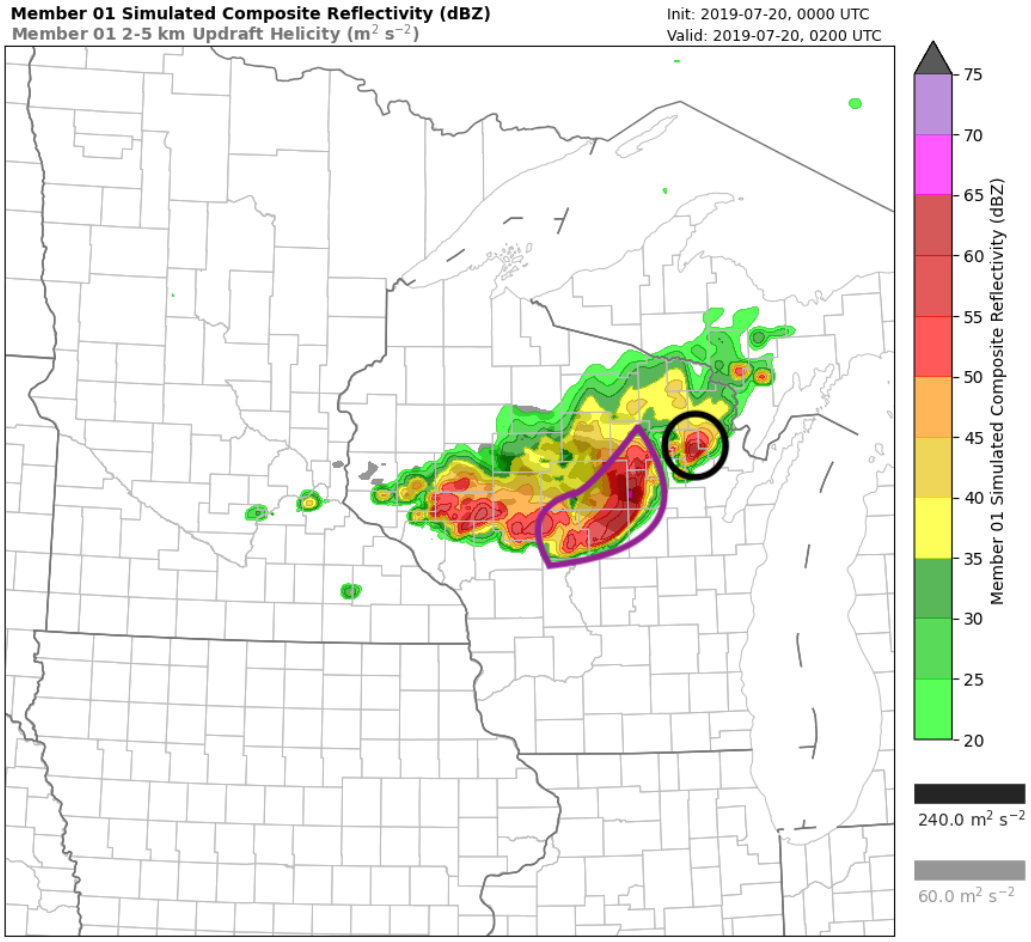

Figure 3.13: 00:00 UTC WoFS forecast of simulated radar reflectivity from WoFS ensemble member 1 valid at 02:00 UTC, which was representative of the ensemble as a whole, showing the supercell (black) east of the developing MCS (purple).

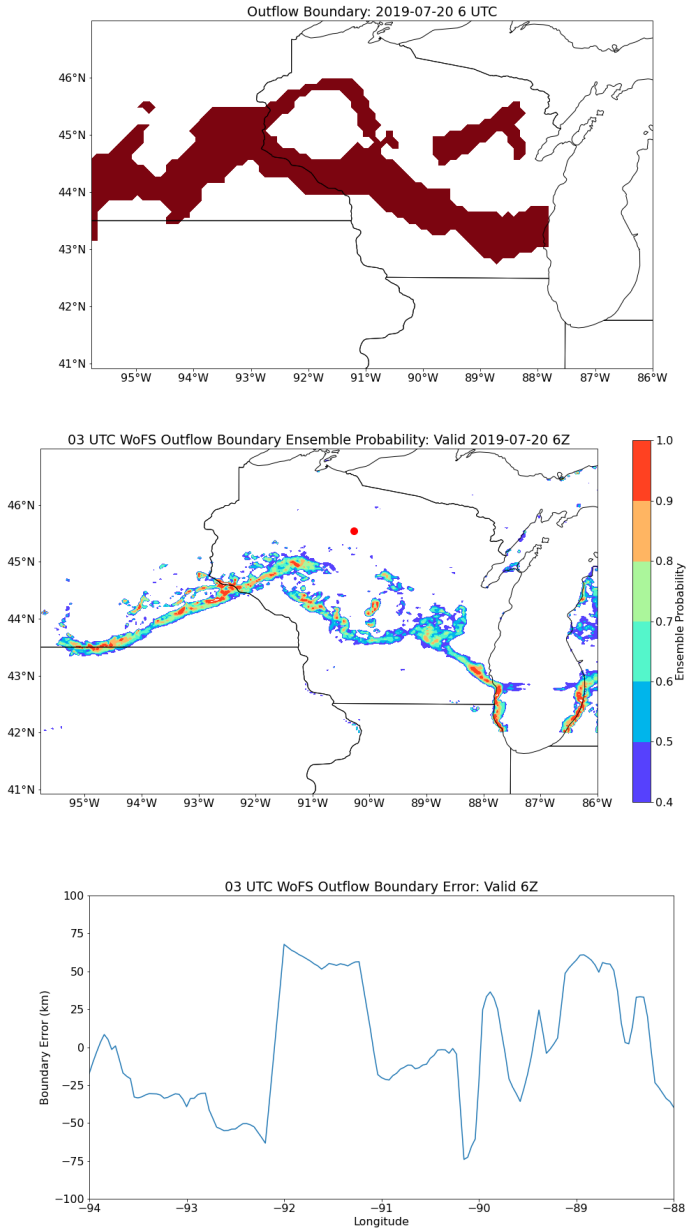

Figure 3.14: Observed location of the outflow boundary at 06:00 UTC on 20 July 2019 (top), with the 03:00 UTC WoFS ensemble probability forecast valid at 06:00 UTC (middle) and WoFS outflow boundary error by longitude (bottom).

Table 3.1: Outflow boundary longitudinally-averaged error from WoFS for each valid hour between 01:00 UTC and 14:00 UTC (by rows), with each of the hourly lead times shown. Positive error shows that WoFS was too far north with the boundary, and vice versa. Red-shaded cells denote runs where WoFS had a southerly boundary bias of at least 25 km, while blue-shaded cells denote runs where WoFS had a northerly boundary bias of at least 10 km.

Lead Time **Valid Hour**	**0 HR**	**1 HR**	**2 HR**	**3 HR**	**4 HR**	**5 HR**	**6 HR**
01:00 UTC	9.86	8.72	4.85	-3.50	-20.26	-9.48	-17.42
02:00 UTC	-8.76	0.40	-4.64	-11.41	-36.75	-33.65	-26.62
03:00 UTC	19.21	1.74	1.94	-15.59	-2.69	-18.16	-29.18
04:00 UTC	4.45	8.07	12.90	7.00	7.52	-4.52	-15.47
05:00 UTC	10.09	9.01	6.82	9.62	15.52	-1.58	-5.16
06:00 UTC	-13.36	-11.88	-8.49	0.39	10.15	13.13	-1.40
07:00 UTC	-15.05	-4.42	-11.24	-4.55	4.96	10.40	-0.41
08:00 UTC	-26.04	-26.30	-17.72	-13.63	-5.50	-1.11	2.57
09:00 UTC	18.82	-23.62	-20.84	-18.52	-18.37	-12.69	-15.84
10:00 UTC	24.32	-19.86	-23.25	-27.02	-28.49	-22.57	-20.62
11:00 UTC	32.35	-35.09	-27.39	-28.74	-34.19	-34.48	-36.79
12:00 UTC	16.73	-17.23	-12.85	-17.26	-27.02	-37.96	-37.05
13:00 UTC	31.04	-24.52	-29.85	-23.29	-21.11	-24.44	-42.70
14:00 UTC	47.40	-39.91	-40.92	-24.49	-28.48	-33.02	-39.37

Notably, WoFS did not exhibit major error magnitudes that would lead to major forecast inaccuracies. Longitude-averaged boundary errors rarely exceeded 30 km, and for none of the 98 model runs studied was average boundary error greater than 50 km. With that said, several trends in WoFS error are worth discussing. For the most part, WoFS had a slight southerly bias. This is indicated by the rather widespread presence of red-shaded cells within Table 3.1 that denoted southerly biases of at least 25 km, as opposed to relatively few blue-shaded cells that denoted northerly biases of at least 10 km. WoFS bias was not uniformly to the south, however. Forecasts valid early in the evening, while the outflow boundary was still traveling southward across the state of Wisconsin, exhibited low error magnitudes. Across many of these early-evening instances, WoFS forecasts tended toward positive bias, meaning that the ensemble was too far north with the southward motion of the outflow boundary through the averaged domain. Later in the evening toward daybreak, as the outflow boundary halted and reversed northward across the averaged domain, the character of WoFS boundary error shifted. The magnitude of average boundary error increased, reaching 30 or more km at times. Furthermore, model bias became more uniformly negative for later valid times. Given that this shift in average model bias occurred as the outflow boundary was stalling and moving northward, this southward bias points toward WoFS being too conservative with the stall and northward return of the outflow boundary.

Visual inspection of Table 3.1 showed that there was often little or no improvement in average error magnitude with decreased lead time. On several instances, the zero-hour WoFS forecast was a worse judge of outflow boundary location than the six-hour forecast for that valid time. Considerable inertia existed within WoFS boundary forecasts—if a WoFS forecast for a certain valid

hour had a strong negative bias, the following WoFS forecasts for the same valid hour were also likely to have a strong negative bias. This autocorrelation provides strong evidence that WoFS forecasts were unlikely to self-correct outflow boundary biases with decreasing lead time as the model assimilated new observations.

3.4 Discussion

3.4.1 Regime 1: Tornadic Supercell

WoFS zero-hour forecasted boundary layer wind profiles at the Prentice radar wind profiler site contained key errors compared to observed profiles from the radar site. WoFS model zero-hour forecasts maintained easterly near-surface winds through a much deeper layer than the radar wind profiler observed. WoFS zero-hour forecasts also developed southerly wind shear with time with height; the Prentice wind profiler, by contrast, maintained minimal meridional wind shear with height. These WoFS errors increased in magnitude as the supercell approached the site.

WoFS is a tool designed to help operational forecasters identify convective hazards on short timescales, so it is useful to consider how WoFS errors may have precluded a forecaster's ability to accurately diagnose and act upon the short-term forecast. Practically speaking, WoFS forecast errors impacted the diagnostic utility of forecast output in the near-storm environment ahead of the tornadic supercell. A forecaster viewing WoFS wind profiles at 21:00 UTC would have had a reasonable sense of the environment out ahead of the supercell. However, as the supercell approached the site, WoFS would have shown much more low-level shear in the near-storm environment than observations.

Therefore, forecasters using this information would be likely to overestimate the potential for tornadoes within the supercell—particularly the potential for significant (EF-2+) tornadoes. While the storm did produce two tornadoes, both of them were EF-0, likely due to the weaker-than-forecast low-level shear.

Potential confounding factors in this research include the low temporal resolution of the Prentice wind profiler, which averaged wind profiles hourly compared to the instantaneous WoFS forecasts. Furthermore, the profiler had a vertical resolution of 57 meters (high-resolution) and 97 meters (low-resolution). WoFS profiles showed large low-level shear in the surface layer, which may have been too fine of a detail for the radar wind profiler to accurately depict and contributed to some of the low-level shear differences. Given that this is a case study, it is prudent to draw conclusions only for this case rather than considering the results as canonical.

With that said, the results are robust enough that we can conclude that WoFS truly overestimated low-level shear in the near-storm environment prior to supercell passage. Given supercell motion near due-east, the low-level shear as depicted in the WoFS forecasted hodographs would largely have been streamwise, promoting high values of storm-relative helicity (SRH). A previous WoFS verification study performed by Laser et al. (2022) found that near-storm SRH was often underestimated near supercells by WoFS compared to Doppler lidar. That study was conducted in the Great Plains with a lidar that had much higher temporal resolution. Furthermore, the supercells studied by Laser et al. (2022) were frequently significantly tornadic and inflow-dominant, meaning that near-storm modification of the low-level wind environment may have played a role in WoFS under-estimating near-storm SRH (Nowotarski and Markowski 2016). It is possible that since the 19 July 2019 supercell was only weakly tornadic, it

was less inflow-dominant than the supercells studied in the Laser et al. (2022) work. Alternatively, it is possible that WoFS biases towards too little low-level shear on the Great Plains where the previous study was conducted, while it biases towards too much low-level shear in the Upper Midwest. Boundary-layer feedbacks may strengthen the argument for either of these explanations, and are discussed in more detail in Chapter 4. Further study with more cases would be required to establish that potential relationship.

3.4.2 Regime 2: Supercell-MCS Merger

As previously mentioned, it is useful to consider how WoFS errors may have precluded a forecaster's ability to accurately diagnose and act upon the short-term forecast. In the case of the blowdown, the impact of those errors was straightforward. A forecaster would be likely to focus on the wrong feature within the MCS for the greatest potential for damaging winds. WoFS had a pronounced signal for enhanced damaging wind gusts within the bow echo south of the developing bookend vortex. However, within the bow echo there was a lesser swath of damaging wind reports. There is some inherent uncertainty in estimating the strength of winds within convection from damaging wind reports received. However, the sheer magnitude of damage within the bookend vortex blowdown region lends confidence that this was the region of highest impact.

The blowdown's occurrence was coincident with a bookend vortex developing; therefore, the blowdown was likely dependent upon the development of the vortex. Often, the development of a bookend vortex is a precursor to enhanced outflow wind potential further south within the bow echo as a rear-inflow jet develops (Wakimoto et al. 2006). This is the scenario favored by the 00:00 UTC WoFS run. However, previous studies have shown that when an MCS and

supercell interact, the resulting bookend vortex may be the most hazardous feature within the MCS (Sieveking and Przybylinski 2003). This appears to be what occurred on 19-20 July 2019. Storm interactions remain a focus of study due to their low predictability as well as their impacts on storm morphology. This case is an example of the difficulties which forecasters and weather models face in forecasting convective hazards during and after storm mergers. The main takeaway from WoFS performance within this convective regime is that storm mergers, particularly those between a supercell and the northern bookend-vortex-favored flank of an MCS, should be treated as low-predictability events even with WoFS as a forecast tool.

3.4.3 Regime 3 - Outflow Boundary

WoFS verification was performed for the outflow boundary across central Wisconsin from 01:00 UTC to 14:00 UTC on 20 July 2019. Ensemble outflow boundary probabilities from the model using a fuzzy logic thresholding algorithm of mass convergence and moisture gradient were compared to the observed outflow boundary determined using the same fuzzy logic thresholding algorithm. WoFS forecasts were somewhat under-reactive to changes in the environment. The model often biased too far north with the outflow boundary while it was advancing southward early in the verification period, while it often biased too far south as the boundary stalled and moved northward across western Wisconsin. WoFS was also unlikely to correct errors for a valid hour with decreased lead time. If six-hour WoFS forecasts biased either northward or southward with the outflow boundary compared to observations, then subsequent forecasts were likely to bias in the same direction.

It is important to consider the role that each of these modeled features would play in confounding a forecaster's understanding of the event. In the case of the under-reactive bias that WoFS displayed, Table 1 shows that all WoFS errors were on the order of no more than a few dozen kilometers. Although the longitudinal averaging of the WoFS error may have smoothed out troublesome spots where error was greater than this magnitude, overall confidence is high that WoFS was able to place the outflow boundary roughly where it actually ended up with minimal error. As outflow boundaries are potential targets for initiation of new convection or can increase hazard probability within ongoing convection, WoFS errors may have only missed the preferred location of the redeveloped tornadic storms by at most up to a county, and frequently by less than that. This would likely provide a forecaster with a higher degree of confidence of a focused area of higher probabilities for hazardous severe weather leading up to the 20 July tornadic event. Therefore, the biased errors that WoFS showed in forecasting the outflow boundary were unlikely to impact the overall model usefulness for this event. It is possible that for a similar case where WoFS was under-reactive to boundary accelerations, greater boundary location errors could be realized if those accelerations were more rapid. Additional cases with faster-traveling and more-rapidly-accelerating outflow boundaries would need to be analyzed to confirm that hypothesis.

Similarly, the autocorrelation between WoFS forecasts for a valid hour could potentially impact forecaster situational awareness for a severe weather event. The WoFS, like many other forecast models, assimilates in-situ and remote observations prior to each new run to give the model the most up-to-date state of the atmosphere. However, it is known that assimilating a coarse grid of hourly surface observations often is not enough for a CAM such as WoFS to properly

adjust to rapidly-shifting environmental conditions such as an outflow boundary acceleration (Sobash and Stensrud 2015). Therefore, if a six-hour WoFS forecast was unable to properly forecast the stalling of the outflow boundary over western and central Wisconsin, assimilating surface observations proved to not be particularly helpful in mitigating errors in boundary location. There is some potential that the static error for a valid time was at least partially caused by the coarse resolution of the surface observation network. However, the consistency with which WoFS forecasts maintained similar errors across runs provides confidence that model autocorrelation was strong from hour to hour. Furthermore, the results of this case fit in with other studies that find CAMs perform poorly with data assimilation amid shifting conditions (Gustafsson et al. 2018). Future studies that compiled multiple cases to quantify the degree of autocorrelation between WoFS forecasts for a valid time would be useful to researchers and model developers. Such a study could, for example, quantify the degree that new methods of data assimilation such as clear-air radar or satellite radiance observations could improve model performance.

3.5 Conclusion

The 19-20 July 2019 severe weather event provided a unique opportunity to examine the environmental evolution not just leading up to a severe thunderstorm, but also the environmental recovery after the initial wave of storms and how following convection was impacted. The WoFS ensemble CAM was run for an extended time prior to and following the passage of an MCS across the CHEESEHEAD domain. WoFS boundary layer wind profiles at Prentice contained much more low-level streamwise vorticity than the radar wind profiler

at that location prior to supercell passage. WoFS ensemble outflow boundary probabilities were then compared to observed outflow boundaries following passage of the MCS. WoFS was slow to advance the outflow boundary to the south across Wisconsin early in the overnight period on 20 July. Late overnight, WoFS was slow to stall and return the boundary northward. WoFS forecasts were also unlikely to improve with decreased lead time. The case study nature of this research precludes the drawing of general conclusions about WoFS performance during severe weather events. However, the conclusions drawn about this case provide valuable insight into how WoFS handled a complex forecast and pose opportunities for future research.

Chapter 4

Boundary Layer Influences on Convection Evolution

4.1 Regime 1: Tornadic Supercell

As discussed within Chapter 3, WoFS overestimated low-level shear in advance of the tornadic supercell. This ran counter to the findings of Laser et al. (2022), which found that WoFS underestimated low-level shear in the near-storm inflow of supercells during the TORUS project. Two hypotheses for these conflicting results were offered. Both hypotheses are contextualized by the consideration of ABL-convection feedbacks.

The first hypothesis maintains that WoFS may have underestimated low-level shear during TORUS but overestimated low-level shear on 19 July 2019 because Laser et al. (2022) studied inflow-dominant supercells, while the 19 July 2019 storm was less-inflow-dominant. Inflow-or-outflow-dominance of a storm is linked to several factors. Outflow-dominance is favored in a supercell when the environment contains less streamwise vorticity. More directly tied to ABL process during the CHEESEHEAD project is the influence of ABL static stability on outflow-dominance. Unstable ABLs are directly linked to increased potential for outflow-dominance in a supercell (Rose 1996). In Chapter 2, it was noted that the ABL in northern Wisconsin in the summer of 2019 was

characterized by low static stability. Meanwhile, in the time period of the TORUS project in 2019 that Laser et al. (2022) studied, the Southern Plains were characterized by a moist, tropical airmass similar to the one found in Oklahoma in the summer of 2020 in Chapter 2. The background state of ABL static stability therefore encourages the hypothesis that WoFS overestimated low-level shear in the case of the 19 July 2019 supercell because the less-inflow-dominant state of the supercell fostered less near-storm modulation of the low-level wind field than a more-inflow-dominant storm.

The second hypothesis maintains that WoFS may have underestimated low-level shear on the treeless Great Plains, but over-estimated low-level shear in the heavily wooded region around the CHEESEHEAD domain in northern Wisconsin. This concept that land use could impact model accuracy in depicting the low-level wind fields across two different locations directly ties back into the goals outlined by the CHEESEHEAD project. Land use heterogeneities and roughness length are not specifically within the scope of this project; however, this is another potential avenue toward investigating ABL-convection feedbacks, and provides an opportunity for future research.

4.2 Regime 2: Boundary Layer Mixing and Severe Wind

The supercell/MCS merger on 19 July 2019 caused a localized straight-line wind event southeast of Rhinelander, Wisconsin. Potential for damaging winds was likely enhanced by several factors spanning meso- and convective scales including boundary layer-convection feedbacks. The interaction between the supercell and the MCS overtaking it from the west could have led to the potential

for enhanced severe wind damage. Research of supercell-MCS mergers has found that the potential for damaging wind reports is usually enhanced following the merger of the two (French and Parker 2012). Convective-scale enhancement of damaging wind caused by the merger falls outside of the scope of this study, and instead the focus will be turned toward ABL wind profiles and thermodynamics.

As discussed in Chapter 3, the WoFS ensemble forecasted increasing low-level wind shear at Prentice prior to supercell passage on 19 July. In particular, hodographs from WoFS ensemble means showed increasing streamwise vorticity in the low-level environment (Figures 3.8, 3.9, 3.10). It has long been understood that streamwise low-level vorticity leads to a dominant supercell mode with enhanced tornado potential (Davies-Jones 1984). Thus, forecasters would anticipate a continuance of the tornado threat with the supercell even as the MCS approached. Meanwhile, the radar wind profiler at Prentice found relatively weak low-level shear that contained far less streamwise vorticity. This likely explains why the tornadoes produced by this supercell were relatively weak and short-lived. The boundary-layer wind errors from WoFS may also have masked the significant-wind-gust threat. Wind profiles favoring strong outflow winds from thunderstorms are difficult to ascertain, as they vary based on conditions (Coniglio et al. 2004). However, it has been noted that environments that favor strong outflow-dominance of thunderstorms also favor damaging wind potential (Corfidi et al. 2004). The high-streamwise-vorticity environment outlined by the WoFS ensemble mean would favor inflow-dominant supercells capable of tornadic activity. However, the less-sheared environment sampled by the Prentice wind profiler would support greater outflow-dominance. It is plausible that forecasters using WoFS data during the evening of 19 July

could have underestimated wind damage potential based on an overestimation of the inflow-dominance of the supercell represented by WoFS hodographs.

Damaging wind potential is also modulated by the static stability of the ABL near the storm. As mentioned in the previous section, a more statically unstable environment is more conducive to outflow-dominance and downdraft potential within a thunderstorm (Rose 1996), and subsequently damaging wind potential. As discussed in Chapter 2, the composite ABL across the CHEESEHEAD domain was characterized by low static stability during the afternoon. Figure 4.1 shows a WoFS ensemble mean forecast sounding valid shortly before the blowdown occurred southeast of Rhinelander. There is a developing nocturnal stable layer, which is to be expected with the blowdown occurring after 00:00 UTC. However, above the stable surface layer there is a deep, rather dry, well-mixed boundary layer. This would be highly conducive to damaging outflow winds within the bookend vortex. The coupling between low static stability within the CHEESEHEAD domain and low static stability ahead of the blowdown suggests land-atmosphere feedbacks likely played a role in both features. Figure 2.18 shows the U.S. Drought Monitor just prior to 19-20 July 2019. An area of abnormally dry conditions was noted across parts of the Upper Peninsula of Michigan and adjacent northern Wisconsin, including the CHEESEHEAD domain. Those abnormally dry conditions led to dry soils and a sensible-heating-dominated boundary layer, which would have encouraged low static stability on a regional scale. It is likely that the deep convective mixing found in the ABL in Wisconsin in July 2019 directly influenced the magnitude of the severe wind event southeast of Rhinelander when the MCS and supercell merged.

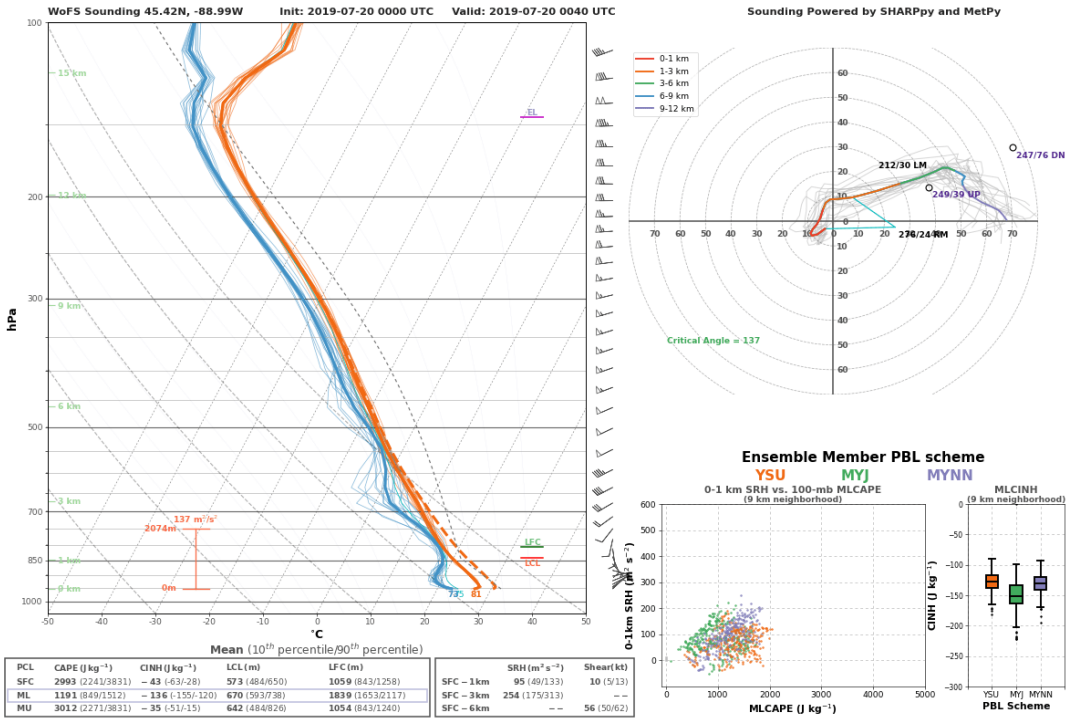

Figure 4.1: 00:00 UTC WoFS ensemble sounding at the region of the blowdown, valid shortly before it occurred.

4.3 Regime 3: Outflow Boundary and the NLLJ

Following the passage of the supercell and MCS on 19 July 2019, the outflow from that convection moved southward across central and southern Wisconsin and Minnesota. Early in the morning hours of 20 July, the outflow stalled and began to return northward across western Wisconsin. As discussed in Chapter 3, this proved to be consequential to convection evolution during the morning of 20 July, when new convection developed along the outflow boundary and produced several morning tornadoes across central Wisconsin. Figure 4.2 shows 850 mb moisture and wind at selected times during the evening of 20 July. Wind at these levels during the summer is influenced by nocturnal and mesoscale factors such as the NLLJ. It is clear from the images that the outflow boundary's southward motion was accompanied by a cold front at the 850 mb level, possibly enhanced by convective outflow.

Strikingly, this front aloft is stalled and also returned north as it meets a belt of strong southerly winds approaching from the central Plains and veering across Iowa. Given the source region, time of night of acceleration, and southerly wind direction, it is quite likely that the belt of southerly winds was the NLLJ (Vanderwende et al. 2015). The NLLJ interacted with a pool of higher moisture across Iowa, transporting it northward into the region that the outflow boundary was moving into in southern Wisconsin and Minnesota. The pool of higher moisture was possibly associated with enhanced evapotranspiration across the state of Iowa, where by mid-July the corn crop is growing. Studies have shown that this enhanced evapotranspiration across Iowa leads to greater near-surface moisture (Matthews 2020). The northward spread of enhanced 850 mb winds

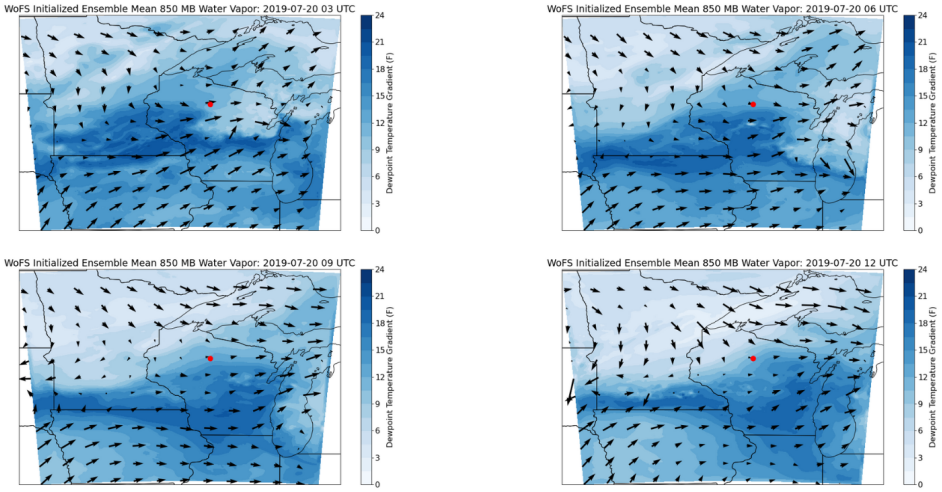

Figure 4.2: WoFS zero-hour forecasts of 850 mb wind (arrows) and water vapor (fill) at 3-hour increments overnight on 19-20 July 2019, showing the development of the NLLJ across western Iowa and its subsequent influence on the motion of the outflow boundary across Wisconsin. The red dot denotes the CHEESEHEAD domain, roughly where the outflow boundary originated.

along the leading edge of the NLLJ coincident with the stall and localized northward return of the outflow boundary suggests that the NLLJ was instrumental in the boundary's behavior. Without the presence of the NLLJ, the morning storms that formed along the outflow boundary may have struggled to remain along the boundary as it continued southward. Furthermore, the NLLJ was most likely instrumental in allowing convection along the outflow boundary to become tornadic. Transport of the moisture reservoir from Iowa, as well as moisture convergence and pooling along the outflow boundary, acted to locally increase moisture within the boundary layer in central and eastern Wisconsin. This allowed a storm to overcome convection inhibition within the more-stable morning boundary layer and produce several tornadoes in rapid succession along the outflow boundary. This provides further evidence of the direct feedbacks between ABL features and convection evolution and hazards during the 19-20 July 2019 severe weather event.

Chapter 5

Conclusion

The atmospheric boundary layer and convective storms are inextricably linked. Convection features and their associated hazards to human life largely occur within the boundary layer, meaning that interactions between the two fields are consequential to meteorologists and the general public. ABL features can influence convection evolution, while features within convection can influence ABL evolution. In spite of this, there is a longstanding tradition within the meteorological realm to consider the two fields as separate entities. This is often grounded in reality; there are opportunities for research purely within the ABL or convection fields. In Chapter 2 of this work, comparison of long-term ABL evolution was performed across three datasets—Wisconsin in the summer, Wisconsin in the fall, and Oklahoma in the summer. This comparison of features established heterogeneities in the response that the ABL had to decreased static stability across two locations: in Wisconsin, the more unstable ABL was found to be less turbulent, while in Oklahoma, the less-unstable ABL was found to be more turbulent. This heterogeneity and its linkage to ABL moisture content addresses the first major research objective of the CHEESEHEAD project: to determine how the ABL responds to heterogeneities in different locations. This objective and the subsequent results fall purely within the ABL field.

In Chapter 3, a verification of WoFS performance during a multiple-regime severe weather event on 19-20 July 2019 occurred. This verification process

established that at times, WoFS had known CAM biases such as its underreactive bias to outflow boundary acceleration, while at other times, WoFS had a bias that ran counter to previous studies (overestimation of low-level shear near the tornadic supercell). The investigation of WoFS tendencies satisfies the goal outlined by NSSL for WoFS as it approaches operational use — for researchers to use a case study method to understand model output better within certain convection regimes. This objective and the subsequent results fall purely within the convection field.

While the results found in Chapters 2 and 3 fell solely within the ABL and convection fields respectively, the results found in those chapters are still able to inform our understanding of the other field. Within Chapter 2, analysis of composite ABL features and their seasonal and spatial variability allowed for greater potential to understand how that ABL would be likely to interact with convection. Within Chapter 3, analysis of WoFS near-storm environments allowed for greater understanding of the model's depiction of near-storm ABL features, and how the model depicts the influence of convection on the ABL. Taken as a whole, the results from Chapters 2 and 3 have greater value to researchers and forecasters than the sum of their parts.

In Chapter 4, the convection features that were studied in Chapter 3 were once more investigated with a focus on influences from ABL features found in Chapter 2. This method not only contextualized the results found in Chapters 2 and 3, it allowed for a deeper understanding of why WoFS outputted certain model solutions, and how those outputs may have impacted forecaster situational awareness. Within regime 1, the tornadic supercell, WoFS zero-hour forecasts overestimated low-level shear in the near-storm inflow to a weakly tornadic supercell. Tornadic potential in supercells is strongly dependent on

ABL wind shear, and this WoFS overestimation may have misled users about the extent of significant tornado potential within this storm. In regime 2, the supercell-MCS merger, it was found that WoFS ensemble maximum wind forecasts missed the location of a significant straight-line wind blowdown by 1-2 counties with as little as 90 minutes of lead time. However, by applying an understanding of ABL evolution, the reasoning for the blowdown became apparent. The low-static-stability ABL that was present in the Wisconsin summer dataset was also present in WoFS proximity soundings, which encouraged strong downdraft winds within the bookend vortex. In regime 3, WoFS was underreactive to the southward acceleration of the outflow boundary early overnight, and then underreactive to the northward acceleration of the outflow boundary during the morning of 20 July 2019. Once again, understanding of ABL evolution in Wisconsin in July 2019 allowed for a greater understanding of convection evolution. The outflow boundary's stall and northward return was influenced by the northward advance of the NLLJ, which pooled moisture along the boundary and allowed for a morning tornado event in Wisconsin on 20 July.

The interconnections between the boundary layer study, convection study, and combined study are shown in Figure 5.1. Exploring the relationship and interconnections between the two fields contains obvious benefit to operational forecasters. If ABL features are detectable within observations or model output, and the impacts of those features are known, a forecaster can better anticipate convection evolution. This is particularly salient given the transient nature of convection hazards—the tornadoes in regime 1 occurred for mere minutes, while the bookend vortex in regime 2 was similarly short-lived. Therefore, connecting the ABL to convection allows forecasters to create mental models that can anticipate outcomes and save valuable time in meeting their important goals of

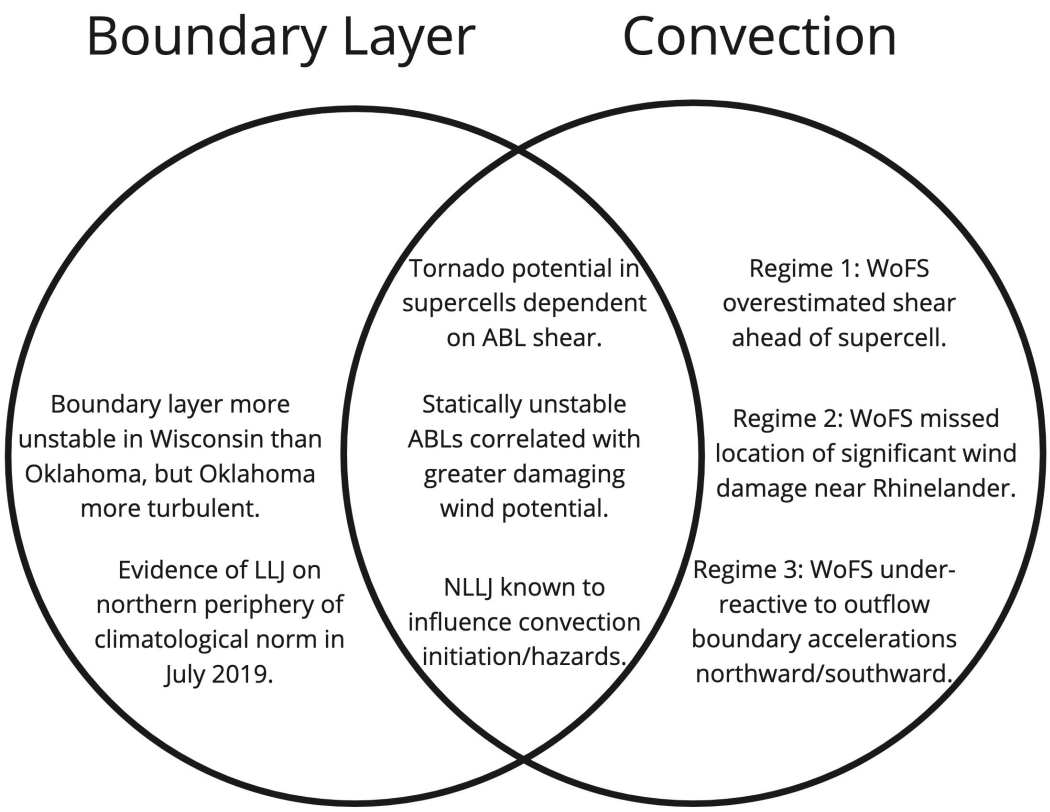

Figure 5.1: A Venn Diagram showing the overlap between ABL and convection features within each convective regime during the 19-20 July 2019 severe weather outbreak in the CHEESEHEAD domain.

protecting lives and property. Investigating the relationship between the ABL and convective storms is clearly beneficial to researchers, as well, for many of the same reasons. Bookend vortices are transient and rare enough that direct, high-quality observations of them are not particularly common. This acts to obscure the relationship between different bookend vortices and their associated hazards. Researchers who are able to apply mental models that anticipate hazard-favorable ABL environments have an advantage in understanding the relationship between convection and hazard.

This work, particularly the WoFS verification study, employs a method that is not meant to be generalized to all situations. The ABL in Norman, Oklahoma may not always be more stable than in Park Falls, Wisconsin in the summer. Comparison of the results of this study to Laser et al. (2022) show that WoFS cannot be relied upon to have a constant low-level shear bias. However, the results of this study inform our understanding of the boundary layer and convection and provide opportunities for future research. Opportunities for future research to build upon the results within the ABL and convective fields have been suggested in Chapters 2 and 3, respectively. There is also an opportunity for cross-disciplinary research from this research. For example, a collection of multiple bookend vortex cases, the associated static stability in near-storm soundings, and maximum observed wind gusts would establish a firm relationship between that convection feature and ABL characteristics. Other opportunities for investigating ABL-convection relationships will arise as focused observations of the ABL during and near convection are collected. The OU Boundary Layer Integrated Sensing and Simulation (BLISS) group is currently collecting those observations for use in analyzing those relationships. BLISS has recently collected ABL data during the TORUS, PERILS, and TRACER projects in and around convection. This study provides proof of the potential benefits of using the data collected by BLISS during those and other projects.

Reference List

Algarra, I., J. Eiras-Barca, G. Miguez-Macho, R. Nieto, and L. Gimeno, 2019: On the assessment of the moisture transport by the great plains low-level jet. *Earth System Dynamics*, **10**, 107–119.

Bell, T. M., B. R. Greene, P. M. Klein, M. Carney, and P. B. Chilson, 2020a: Confronting the boundary layer data gap: evaluating new and existing methodologies of probing the lower atmosphere. *Atmospheric Measurement Techniques*, **13**, 3855–3872.

Bell, T. M., P. Klein, N. Wildmann, and R. Menke, 2020b: Analysis of flow in complex terrain using multi-doppler lidar retrievals. *Atmospheric Measurement Techniques*, **13**, 1357–1371.

Bell, T. M., P. M. Klein, J. K. Lundquist, and S. Waugh, 2021: Remote-sensing and radiosonde datasets collected in the san luis valley during the lapse-rate campaign. *Earth System Science Data*, **13**, 1041–1051.

Bonin, T. A., J. F. Newman, P. M. Klein, P. B. Chilson, and S. Wharton, 2016: Improvement of vertical velocity statistics measured by a doppler lidar through comparison with sonic anemometer observations. *Atmospheric Measurement Techniques*, **9**, 5833–5852.

Bonner, W. D., 1968: Climatology of the low level jet. *Mon. Wea. Rev.*, **96**, 833–850.

Butterworth, B. J., A. R. Desai, P. A. Townsend, G. W. Petty, C. G. Andresen, T. H. Bertram, E. L. Kruger, J. K. Mineau, E. R. Olson, S. Paleri, et al., 2021: Connecting land–atmosphere interactions to surface heterogeneity in cheesehead19. *Bulletin of the American Meteorological Society*, **102**, E421–E445.

Byers, H. R. and L. J. Battan, 1949: Some effects of vertical wind shear on thunderstorm structure. *Bulletin of the American Meteorological Society*, **30**, 168–175.

Carroll, B. J., B. B. Demoz, and R. Delgado, 2019: An overview of low-level jet winds and corresponding mixed layer depths during pecan. *Journal of Geophysical Research: Atmospheres*, **124**, 9141–9160.

Chipilski, H. G., X. Wang, and D. B. Parsons, 2020: Impact of assimilating pecan profilers on the prediction of bore-driven nocturnal convection: A multiscale forecast evaluation for the 6 july 2015 case study. *Monthly Weather Review*, **148**, 1147–1175.

Coniglio, M. C., G. S. Romine, D. D. Turner, and R. D. Torn, 2019: Impacts of targeted aeri and doppler lidar wind retrievals on short-term forecasts of the initiation and early evolution of thunderstorms. *Monthly Weather Review*, **147**, 1149–1170.

Coniglio, M. C., D. J. Stensrud, and M. B. Richman, 2004: An observational study of derecho-producing convective systems. *Weather and forecasting*, **19**, 320–337.

Corfidi, S. F., 1998: Forecasting mcs mode and motion. *Preprints, 19th Conf. on Severe Local Storms, Minneapolis, MN, Amer. Meteor. Soc*, 626–629.

Corfidi, S. F., D. A. Imy, S. J. Taylor, and A. Logan, 2004: P 4.72 a preliminary investigation of derecho-producing mcss in environments of very low dewpoints.

Davies-Jones, R., 1984: Streamwise vorticity: The origin of updraft rotation in supercell storms. *Journal of Atmospheric Sciences*, **41**, 2991–3006.

Degelia, S. K., X. Wang, and D. J. Stensrud, 2019: An evaluation of the impact of assimilating aeri retrievals, kinematic profilers, rawinsondes, and surface observations on a forecast of a nocturnal convection initiation event during the pecan field campaign. *Monthly Weather Review*, **147**, 2739–2764.

Du, Y., G. Chen, B. Han, C. Mai, L. Bai, and M. Li, 2020: Convection initiation and growth at the coast of south china. part i: Effect of the marine boundary layer jet. *Monthly Weather Review*, **148**, 3847 – 3869.

Flournoy, M. D. and M. C. Coniglio, 2019: Origins of vorticity in a simulated tornadic mesovortex observed during pecan on 6 july 2015. *Monthly Weather Review*, **147**, 107–134.

French, A. J. and M. D. Parker, 2012: Observations of mergers between squall lines and isolated supercell thunderstorms. *Weather and forecasting*, **27**, 255–278.

Garner, J., 2013: A study of synoptic-scale tornado regimes. *E-Journal of Severe Storms Meteorology*, **8**.

Gebauer, J. G., E. Fedorovich, and A. Shapiro, 2017: A 1d theoretical analysis of northerly low-level jets over the great plains. *Journal of the Atmospheric Sciences*, **74**, 3419–3431.

Gebauer, J. G., A. Shapiro, E. Fedorovich, and P. Klein, 2018: Convection initiation caused by heterogeneous low-level jets over the great plains.

Geerts, B., D. Parsons, C. L. Ziegler, T. M. Weckwerth, M. I. Biggerstaff, R. D. Clark, M. C. Coniglio, B. B. Demoz, R. A. Ferrare, W. A. Gallus Jr, et al., 2017: The 2015 plains elevated convection at night field project. *Bulletin of the American Meteorological Society*, **98**, 767–786.

Grund, C. J., R. M. Banta, J. L. George, J. N. Howell, M. J. Post, R. A. Richter, and A. M. Weickmann, 2001: High-resolution doppler lidar for boundary layer and cloud research. *Journal of Atmospheric and Oceanic Technology*, **18**, 376–393.

Gustafsson, N., T. Janjić, C. Schraff, D. Leuenberger, M. Weissmann, H. Reich, P. Brousseau, T. Montmerle, E. Wattrelot, A. Bučánek, et al., 2018: Survey of data assimilation methods for convective-scale numerical weather prediction at operational centres. *Quarterly Journal of the Royal Meteorological Society*, **144**, 1218–1256.

Hewson, T. D., 1998: Objective fronts. *Meteorological Applications*, **5**, 37–65.

Huang, M., Z. Gao, S. Miao, F. Chen, M. A. LeMone, J. Li, F. Hu, and L. Wang, 2017: Estimate of boundary-layer depth over beijing, china, using doppler lidar data during surf-2015. *Boundary-Layer Meteorology*, **162**, 503–522.

Huang, Y., Z. Meng, W. Li, L. Bai, and X. Meng, 2019: General features of radar-observed boundary layer convergence lines and their associated convection over a sharp vegetation-contrast area. *Geophysical Research Letters*, **46**, 2865–2873.

Jenkner, J., M. Sprenger, I. Schwenk, C. Schwierz, S. Dierer, and D. Leuenberger, 2010: Detection and climatology of fronts in a high-resolution model reanalysis over the alps. *Meteorological Applications: A journal of forecasting, practical applications, training techniques and modelling*, **17**, 1–18.

Jiang, X., N.-C. Lau, I. M. Held, and J. J. Ploshay, 2007: Mechanisms of the great plains low-level jet as simulated in an agcm. *Journal of the Atmospheric Sciences*, **64**, 532–547.

Klein, P., T. Bell, and E. Smith, 2020: Clamps1 tropoe retrieved thermodynamic profiles. version 1.0.
URL `https://data.eol.ucar.edu/dataset/592.089`

Kolmogorov, A. N., 1941: The local structure of turbulence in incompressible viscous fluid for very large reynolds numbers. *Cr Acad. Sci. URSS*, **30**, 301–305.

Lamraoui, F., J. F. Booth, C. M. Naud, M. P. Jensen, and K. L. Johnson, 2019: The interaction between boundary layer and convection schemes in a

wrf simulation of post cold frontal clouds over the arm east north atlantic site. *Journal of Geophysical Research: Atmospheres*, **124**, 4699–4721.

Laser, J. J., M. C. Coniglio, P. S. Skinner, and E. N. Smith, 2022: Doppler lidar and mobile radiosonde observation-based evaluation of warn-on-forecast system predicted near-supercell environments during torus 2019. *Weather and Forecasting*.

Lee, T. R., M. Buban, D. D. Turner, T. P. Meyers, and C. B. Baker, 2019: Evaluation of the high-resolution rapid refresh (hrrr) model using near-surface meteorological and flux observations from northern alabama. *Weather and Forecasting*, **34**, 635–663.

Lenschow, D., J. C. Wyngaard, and W. T. Pennell, 1980: Mean-field and second-moment budgets in a baroclinic, convective boundary layer. *Journal of Atmospheric Sciences*, **37**, 1313–1326.

Lenschow, D. H., M. Lothon, S. D. Mayor, P. P. Sullivan, and G. Canut, 2012: A comparison of higher-order vertical velocity moments in the convective boundary layer from lidar with in situ measurements and large-eddy simulation. *Boundary-layer meteorology*, **143**, 107–123.

Lin, G., C. Grasmick, B. Geerts, Z. Wang, and M. Deng, 2021: Convection initiation and bore formation following the collision of mesoscale boundaries over a developing stable boundary layer: A case study from pecan. *Monthly Weather Review*, **149**, 2351–2367.

Maddox, R. A., 1983: Large-scale meteorological conditions associated with midlatitude, mesoscale convective complexes. **111**, 1475–1493.

Matthews, L. R., 2020: *Corn Sweat: A Qualitative and Hydrologic Analysis of a High Resolution Evapotranspiration Model in Iowa*. Ph.D. thesis, The University of Iowa.

McCann, D. W. and J. P. Whistler, 2001: Problems and solutions for drawing fronts objectively. *Meteorological Applications*, **8**, 195–203.

Monin, A. S. and A. M. Obukhov, 1954: Basic laws of turbulent mixing in the surface layer of the atmosphere. *Contrib. Geophys. Inst. Acad. Sci. USSR*, **151**, e187.

Mueller, C. K. and R. E. Carbone, 1987: Dynamics of a thunderstorm outflow. *Journal of the Atmospheric sciences*, **44**, 1879–1898.

Nowotarski, C. J. and P. M. Markowski, 2016: Modifications to the near-storm environment induced by simulated supercell thunderstorms. *Monthly Weather Review*, **144**, 273–293.

O'Gorman, P. and C. J. Muller, 2010: How closely do changes in surface and column water vapor follow clausius–clapeyron scaling in climate change simulations? *Environmental Research Letters*, **5**, 025207.

Parfitt, R., A. Czaja, and H. Seo, 2017: A simple diagnostic for the detection of atmospheric fronts. *Geophysical Research Letters*, **44**, 4351–4358.

Pichugina, Y. L., R. Banta, T. Bonin, W. Brewer, A. Choukulkar, B. McCarty, S. Baidar, C. Draxl, H. Fernando, J. Kenyon, et al., 2019: Spatial variability of winds and hrrr–ncep model error statistics at three doppler-lidar sites in the wind-energy generation region of the columbia river basin. *Journal of Applied Meteorology and Climatology*, **58**, 1633–1656.

Pinto, J. O., J. A. Grim, and M. Steiner, 2015: Assessment of the high-resolution rapid refresh model's ability to predict mesoscale convective systems using object-based evaluation. *Weather and Forecasting*, **30**, 892–913.

Pitchford, K. L. and J. London, 1962: The low-level jet as related to nocturnal thunderstorms over Midwest United States. **1**, 43–47.

Prandtl, L., 1904: Über flussigkeitsbewegung bei sehr kleiner reibung. *Verhandl. III, Internat. Math.-Kong., Heidelberg, Teubner, Leipzig, 1904*, 484–491.

Rose, M. A., 1996: Downbursts. *Nat'l. Wea. Digest*, Citeseer.

Sanders, F. and C. A. Doswell, 1995: A case for detailed surface analysis. *Bulletin of the American Meteorological Society*, **76**, 505–522.

Schemm, S., I. Rudeva, and I. Simmonds, 2015: Extratropical fronts in the lower troposphere–global perspectives obtained from two automated methods. *Quarterly Journal of the Royal Meteorological Society*, **141**, 1686–1698.

Shapiro, M. A. and D. Keyser, 1990: Extratropical cyclones. *The Erik Palmén Memorial Volume, Chapt."Fronts, Jet Streams and the Tropopause", American Meteorological Society, Boston, MA*, 167–191.

Sieveking, J. E. and R. W. Przybylinski, 2003: 7a. 5 the interaction of a hp supercell thunderstorm and bow echo to produce a prolonged severe wind event in east central missouri.

Skinner, P. S., D. M. Wheatley, K. H. Knopfmeier, A. E. Reinhart, J. J. Choate, T. A. Jones, G. J. Creager, D. C. Dowell, C. R. Alexander, T. T. Ladwig, L. J. Wicker, P. L. Heinselman, P. Minnis, and R. Palikonda, 2018: Object-based verification of a prototype warn-on-forecast system. *Weather and Forecasting*, **33**, 1225 – 1250.

Smith, E. N., J. G. Gebauer, P. M. Klein, E. Fedorovich, and J. A. Gibbs, 2019: The great plains low-level jet during pecan: Observed and simulated characteristics. *Monthly Weather Review*, **147**, 1845–1869.

Smith, E. N., B. R. Greene, T. M. Bell, W. G. Blumberg, R. Wakefield, D. Reif, Q. Niu, Q. Wang, and D. D. Turner, 2021: Evaluation and applications of multi-instrument boundary-layer thermodynamic retrievals. *Boundary-Layer Meteorology*, **181**, 95–123.

Sobash, R. A. and D. J. Stensrud, 2015: Assimilating surface mesonet observations with the enkf to improve ensemble forecasts of convection initiation on 29 may 2012. *Monthly Weather Review*, **143**, 3700–3725.

Stensrud, D. J., L. J. Wicker, M. Xue, D. T. Dawson, N. Yussouf, D. M. Wheatley, T. E. Thompson, N. A. Snook, T. M. Smith, A. D. Schenkman, C. K. Potvin, E. R. Mansell, T. Lei, K. M. Kuhlman, Y. Jung, T. A. Jones, J. Gao, M. C. Coniglio, H. E. Brooks, and K. A. Brewster, 2013: Progress and challenges with warn-on-forecast. *Atmospheric Research*, **123**, 2–16, 6th European Conference on Severe Storms 2011. Palma de Mallorca, Spain.

Stern, H. and N. E. Davidson, 2015: Trends in the skill of weather prediction at lead times of 1–14 days. *Quarterly Journal of the Royal Meteorological Society*, **141**, 2726–2736.

Stull, R., 1988: *An Introduction to Boundary Layer Meteorology*. Atmospheric and Oceanographic Sciences Library, Springer Netherlands.
URL `https://books.google.com/books?id=eRRz9RNvNOkC`

Turner, D. D., S. A. Clough, J. C. Liljegren, E. E. Clothiaux, K. E. Cady-Pereira, and K. L. Gaustad, 2007: Retrieving liquid water path and precipitable water vapor from the atmospheric radiation measurement (arm) microwave radiometers. *IEEE Transactions on Geoscience and Remote Sensing*, **45**, 3680–3690.

Turner, D. D. and U. Löhnert, 2021: Ground-based temperature and humidity profiling: combining active and passive remote sensors. *Atmospheric Measurement Techniques*, **14**, 3033–3048.

Vanderwende, B. J., J. K. Lundquist, M. E. Rhodes, E. S. Takle, and S. L. Irvin, 2015: Observing and simulating the summertime low-level jet in central iowa. *Monthly Weather Review*, **143**, 2319–2336.

W., P. J. F., 1982: Subjective interpretation of geostationary satellite data for nowcasting. *Nowcasting*, 149–166.
URL `https://cir.nii.ac.jp/crid/1571135649743402880`

Wagner, T., 2021: Ssec sparc doppler lidar at wlef. version 1.0. URL https://data.eol.ucar.edu/dataset/592.143

Wagner, T. J., P. M. Klein, and D. D. Turner, 2019: A new generation of ground-based mobile platforms for active and passive profiling of the boundary layer. *Bulletin of the American Meteorological Society*, **100**, 137–153.

Wakimoto, R. M., H. V. Murphey, A. Nester, D. P. Jorgensen, and N. T. Atkins, 2006: High winds generated by bow echoes. part i: Overview of the omaha bow echo 5 july 2003 storm during bamex. *Monthly weather review*, **134**, 2793–2812.

Wanner, L. and M. Mauder, 2020: Kit wind lidar at wlef. version 1.0. URL https://data.eol.ucar.edu/dataset/592.024

Weckwerth, T. and D. Parsons, 2002: An overview of the international h2o project (ihop2002). *Preprints, 21st Conf. on Severe Local Storms, San Antonio, TX, Amer. Meteor. Soc*, 279–282.

Weisman, M. L. and J. B. Klemp, 1984: The structure and classification of numerically simulated convective storms in directionally varying wind shears. *Monthly Weather Review*, **112**, 2479–2498.

Wilczak, J. and D. Gottas, 2020: Noaa psl radar wind profiler, radio acoustic sounding system, and surface meteorology data. version 2.0. URL https://data.eol.ucar.edu/dataset/592.026

Wilson, J. W. and W. E. Schreiber, 1986: Initiation of convective storms at radar-observed boundary-layer convergence lines. *Monthly Weather Review*, **114**, 2516–2536.

Wu, Y. and S. Raman, 1998: The summertime great plains low level jet and the effect of its origin on moisture transport. *Boundary-Layer Meteorology*, **88**, 445–466.

Yue, H. and M. Gebremichael, 2020: Evaluation of high-resolution rapid refresh (hrrr) forecasts for extreme precipitation. *Environmental Research Communications*, **2**, 065004.

Zhao, B., J. Zhen, C. Hu, J. Du, Y. Zhu, and C. Zhang, 1992: Study on clouds and marine atmospheric boundary layer. *Advances in atmospheric sciences*, **9**, 383–396.